Acta Pharmaceutica Sinica B 2026;16(8):5452−5470

Chinese Pharmaceutical Association
Institute of Materia Medica, Chinese Academy of Medical Sciences

Acta Pharmaceutica Sinica B

www.elsevier.com/locate/apsb
www.sciencedirect.com

ORIGINAL ARTICLE

Targeted nanoparticles with triggered lysosomal escape enable anti-angiogenic immunotherapy for peritoneal metastatic colorectal cancer

Meng Wang[a,†], Yutong Qian[a,†], Yicong Li[a], Xicheng Li[a], Mei Zhu[a], Danrong Hu[b], Ran Li[b], Meng Pan[a], Yun Yang[a], Jianan Li[a], Zhiyong Qian[a,*]

[a]*Institute of Biomaterials and Nanomedicine, Department of Biotherapy, Cancer Center and State Key Laboratory of Biotherapy, West China Hospital, Sichuan University, Chengdu 610041, China*
[b]*Rehabilitation Medicine Center and Institute of Rehabilitation Medicine, Key Laboratory of Rehabilitation Medicine in Sichuan Province, West China Hospital, Sichuan University, Chengdu 610041, China*

Received 21 September 2025; received in revised form 24 December 2025; accepted 13 January 2026

KEY WORDS

Peritoneal metastatic colorectal cancer;
Anti-angiogenic immunotherapy;
Endocytosis;
Lysosomal escape;
Folic acid;
Phenylboronic acid;
Regorafenib;
DMXAA

Abstract Peritoneal metastatic colorectal cancer (PMC) is highly aggressive and resistant to anti-angiogenic monotherapy due to the angiogenesis−immunosuppression vicious cycle. This study develops dual-ligand modified nanoparticles (Reg/DMX@BPF NPs), co-loaded with the angiogenesis inhibitor regorafenib (Reg) and the stimulator of interferon genes (STING) agonist DMXAA (DMX). Reg prevents DMX aggregation as a molecular scaffold *via* $\pi-\pi$ stacking. The folic acid (FA) and phenylboronic acid (PBA)-functionalized BSA (BPF) facilitates active tumor targeting and metastatic site enrichment. Upon internalization into lysosomes, the acidic pH triggers boronate ester bond formation between PBA and glycoproteins, inducing lysosomal disruption and efficient cytosolic release. In addition to STING activation, the BPF potently activates toll-like receptor 4 signaling, synergistically inducing M1 tumor-associated macrophages polarization and dendritic cells maturation. *In vivo* results demonstrate that Reg/DMX@BPF NPs synergistically inhibit tumor proliferation, normalize pathological vasculature, and reprogram the immunosuppressive microenvironment, which leads to reduced tumor burden and ascites. Collectively, the targeted lysosome-escape nanoparticles provide a novel strategy to overcome the poor efficacy of anti-angiogenic therapy against PMC.

*Corresponding author.
E-mail address: anderson-qian@163.com (Zhiyong Qian).
[†]These authors made equal contributions to this work.
Peer review under the responsibility of Chinese Pharmaceutical Association and Institute of Materia Medica, Chinese Academy of Medical Sciences.

https://doi.org/10.1016/j.apsb.2026.04.016

1. Introduction

Peritoneal metastatic colorectal cancer (PMC) is a highly aggressive form of metastasis, threatening approximately 15% of patients at initial diagnosis and 40% of those with recurrent disease[1-3]. Tumor cells disseminate from the primary site, invade the peritoneal cavity, and rely on aberrant peritoneal vasculature for nutrient and oxygen supply, fueling metastatic growth[4-6]. Despite cytoreductive surgery, patients with residual tumors larger than 2.5 mm face a median survival of less than 7 months due to rapid disease progression and associated complications[7,8].

Anti-angiogenic therapies, such as bevacizumab, target vascular endothelial growth factor (VEGF) to delay disease progression[9]. However, their efficacy is limited by compensatory neovascularization and an immunosuppressive tumor microenvironment (TME)[10,11]. Aberrant vasculature induces hypoxia, upregulating hypoxia-inducible factor-1α, which boosts VEGF and colony-stimulating factor 1 expression[12-14]. VEGF not only drives angiogenesis but also exerts well-documented immunosuppressive effects, including impairing dendritic cells (DCs) maturation and function, suppressing cytotoxic T cells expansion, and recruiting myeloid-derived suppressor cells into tumors[15-18]. Meanwhile, colony-stimulating factor 1 recruits M2 tumor-associated macrophages (TAMs), which exacerbate vascular dysfunction by additional VEGF secretion[19-21]. Furthermore, interstitial hypertension and angiogenic endothelial cells hinder drug delivery and $CD8^+$ T cells infiltration by enhancing barrier functions[22,23]. Collectively, this vascular−immune crosstalk establishes a vicious cycle that highlights the need for multidimensional therapeutic strategies.

Therefore, the combination of anti-angiogenic agents and immunotherapy represents a promising strategy to address this complex pathological network[24]. For instance, the multi-kinase inhibitor regorafenib (Reg) inhibits vascular endothelial growth factor receptor 2 (VEGFR2) and RAF, thereby suppressing pathological angiogenesis and tumor proliferation[25]. Concurrently, activating the stimulator of interferon genes (STING) pathway is critical for eliciting robust antitumor immunity[26,27]. The STING agonist DMXAA (DMX) activates this pathway in tumor-associated immune cells, promoting M1 polarization of TAMs and enhancing DCs maturation[28,29]. However, clinical challenges persist: oral administration of Reg suffers from limited tumor accumulation due to first-pass metabolism and the plasma-peritoneum barrier, while DMX's rigid planar xanthone core causes aggregation in aqueous environments, complicating its incorporation into nanoparticles[30-32].

Nanotechnology offers a versatile platform for integrating multiple therapeutic strategies through rational design[33-36]. In this context, bovine serum albumin (BSA) has been extensively explored as a biocompatible and biodegradable nanocarrier, owing to its natural abundance, low immunogenicity, and high drug-loading capacity[37,38]. Nevertheless, native BSA lacks specific targeting capabilities, limiting its efficacy in the heterogeneous TME[39,40]. Importantly, the abundant amino and carboxyl groups on BSA surfaces allow covalent modifications to improve tumor penetration and intracellular drug release. For example, folic acid (FA) has been widely utilized for its high affinity to folate receptors (FRα/β), which are overexpressed on cancer cells and TAMs[41,42]. Additionally, phenylboronic acid (PBA) enhances tumor-selective accumulation and facilitates lysosomal escape by forming pH-responsive boronate esters with sialic acid (SA) on tumor cells or glycoproteins on lysosomal membranes[43-47].

In this study, we aimed to develop a novel nanoplatform to simultaneously disrupt the angiogenic and immunosuppressive pathways (Fig. 1). Our primary objective was to construct a dual-ligand modified BSA-based NPs (Reg/DMX@BPF NPs) for the co-delivery of Reg and DMX. This platform integrates several innovative features: First, Reg serves as a molecular scaffold to stabilize DMX *via* $\pi-\pi$ stacking, overcoming its inherent aggregation propensity and achieving high co-loading efficiency. The BSA is then functionalized with FA and PBA to enable active tumor targeting and metastatic site enrichment. Subsequently, the PBA moiety facilitates triggered lysosomal escape *via* membrane disruption, ensuring efficient cytosolic delivery of DMX. Interestingly, the engineered BPF carrier itself possesses intrinsic immunostimulatory properties that activate the TLR4/NF-κB pathway. This multifaceted design enables the nanoplatform to synergistically inhibit tumor proliferation, normalize pathological vasculature, and activate antitumor immunity. Specifically, treatment with Reg/DMX@BPF NPs led to a dramatic reduction in tumor burden (0.13 ± 0.05 g *vs.* 1.55 ± 0.34 g in the control group), representing a 92% inhibition. This was accompanied by a complete prevention of ascites formation, a significant enhancement of $CD8^+$ T cells infiltration, and effective polarization of TAMs towards the anti-tumor M1 phenotype. Collectively, these findings demonstrate that the targeted lysosome-escape nanoparticles provide a novel and effective therapeutic paradigm for overcoming the poor efficacy of anti-angiogenic therapy against PMC.

2. Materials and methods

2.1. Reagents

Bovine serum albumin (BSA) was purchased from Absin Bioscience Inc. (Shanghai, China). 4-Carboxyphenylboronic acid (PBA) and folic acid (FA) were purchased from Aladdin Biochemical Technology Co., Ltd., (Shanghai, China). Regorafenib (Reg), DMXAA (DMX), CCK-8 cell proliferation kit, Chlorin e6 (Ce6), and Coumarin 6 (Cou6) were provided by MedChemExpress (Monmouth Junction, NJ, USA). RPMI 1640, Endothelial Cell Medium (ECM), Dulbecco's modified Eagle's medium (DMEM), fetal bovine serum (FBS), and penicillin−streptomycin solution were acquired from Gibco (Thermo Fisher Scientific, Waltham, MA, USA). The Recombinant murine cytokines (M-CSF, IL-4, and GM-CSF) were obtained from Novoprotein Scientific Inc. (Suzhou, China). Mouse TNF-α and IL-6 ELISA kits were produced by Lianke Biotechnology Co., Ltd., (Hangzhou, China). Antibodies for flow cytometry were from BioLegend (San Diego, CA, USA).

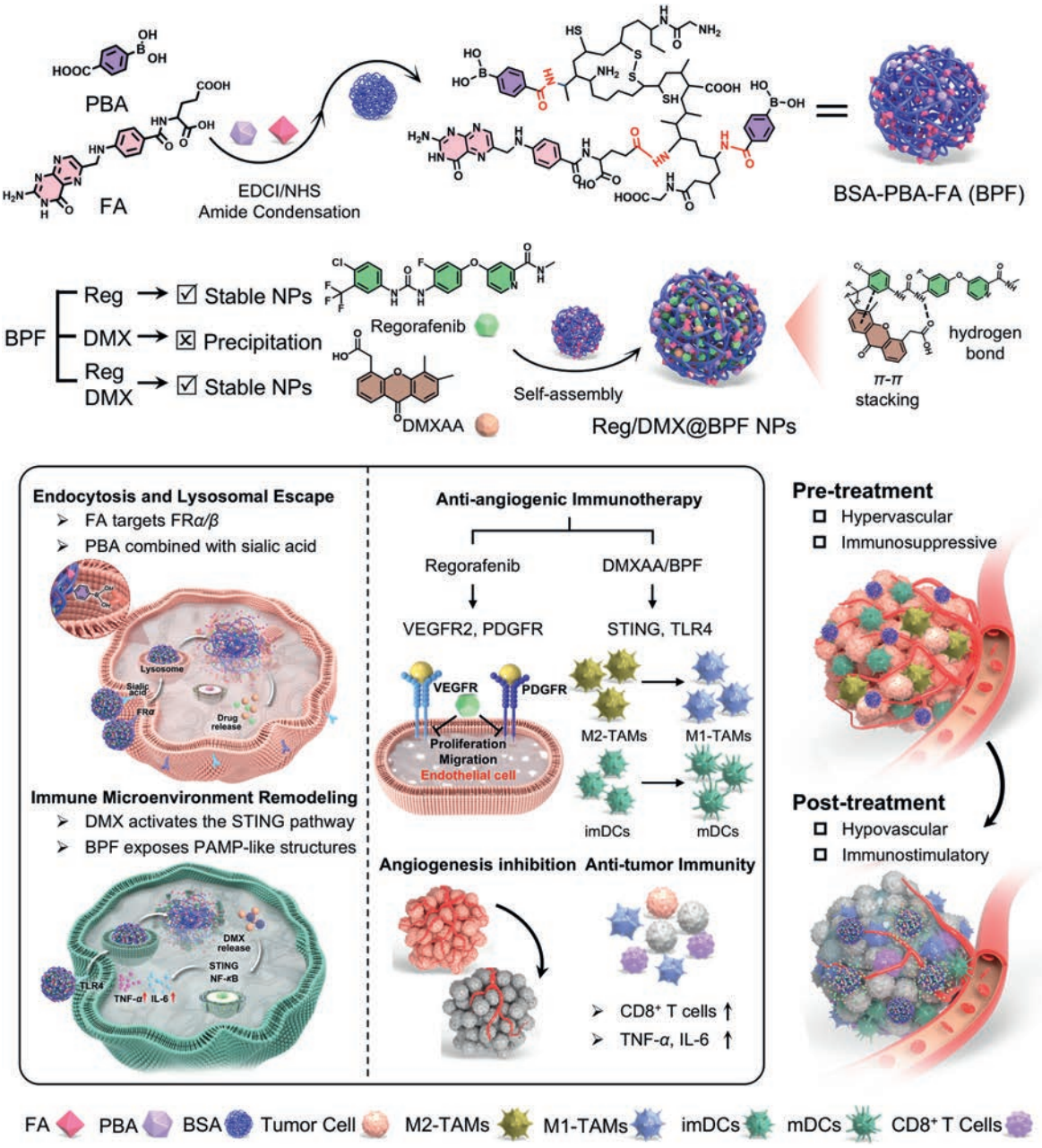

Figure 1 Schematic illustration of engineered Reg/DMX@BPF NPs enabling tumor-targeted delivery, where phenylboronic acid (PBA) facilitates lysosomal escape, thereby synergistically disrupting the angiogenesis−immunosuppression vicious cycle in peritoneal metastatic colorectal cancer.

D-Luciferin potassium salt was supplied by Yusen Biotechnology Co., Ltd., (Shanghai, China). All chemicals were used as received without further purification.

2.2. *Cells and animals*

Luciferase-labeled CT26 colorectal cancer cells (CT26-luc), human umbilical vein endothelial cells (HUVECs), and human immortalized keratinocytes (HaCaTs) were cultured in RPMI 1640, ECM, or DMEM, respectively. Each medium was supplemented with 10% FBS and 1% penicillin−streptomycin. Cells were maintained at 37 °C under a humidified atmosphere containing 5% CO_2 atmosphere and passaged routinely.

Bone marrow-derived macrophages (BMDMs) and bone marrow-derived dendritic cells (BMDCs) were isolated from C57BL/6 mice. For BMDMs, bone marrow cells were cultured in DMEM with 20 ng/mL M-CSF for 6 to 7 days, then polarized to M2 phenotype with IL-4 (20 ng/mL) for 24 h. For BMDCs, bone marrow cells were cultured in RPMI-1640 medium with 10% FBS, 20 ng/mL GM-CSF, and 10 ng/mL IL-4 for 7 days, with half-medium changes every 2 days.

Female BALB/c mice (6−8 weeks old, 20 ± 2 g) were purchased from GemPharmatech Co., Ltd., (Jiangsu, China). Mice were housed under specific pathogen-free conditions (temperature, 26 °C; humidity, 50% to 60%; 12-h light/dark cycle) with free access to food and water. All animal experiments were approved

by the Experimental Animal Ethics Committee of the State Key Laboratory of Biotherapy, Sichuan University (Approval No. 20241127009) and performed in accordance with AAALAC International standards for laboratory animal welfare.

2.3. Synthesis and characterization of BSA-PBA-FA (BPF)

PBA and FA were dissolved in dimethyl sulfoxide (DMSO), and the carboxyl groups were activated with 1-ethyl-3-(3-dimethylaminopropyl) carbodiimide (EDCI) and *N*-hydroxy succinimide (NHS). The activated solution was added to the BSA solution and stirred at 25 °C for 24 h in the dark. The reaction mixture was transferred to a dialysis bag (molecular weight cutoff [MWCO], 3.5 kDa) and dialyzed against ultrapure water for 48 h, with water changes every 8 h. Insoluble impurities were removed by filtration through a 0.8-μm membrane. The purified product was freeze-dried to yield the BPF nanocarrier, which was stored at −20 °C.

The conjugation of FA and PBA was confirmed by ultraviolet−visible (UV−vis) absorption and ARS analysis. Fourier transform infrared (FTIR) spectroscopy provided insights into functional groups. Proton nuclear magnetic resonance (^{1}H NMR) spectra were carried out to compare chemical shifts between BSA and BPF. Sulfur (from BSA) and boron (from PBA) contents were quantified by inductively coupled plasma mass spectrometry (ICP-MS) to calculate the PBA modification ratio. MALDI-TOF-MS (positive ion mode, sinapic acid as matrix) was used to determine molecular weight changes, and FA loading capacity was calculated from the mass difference. Biocompatibility was evaluated by a hemolysis assay using saline, BSA, BPF, and deionized water as controls.

2.4. Preparation and characterization of nanoparticles

Preparation of Reg/DMX@BPF NPs. Reg and DMX were dissolved in DMSO to prepare a 10 mg/mL stock solution. BPF nanocarrier and polyvinylpyrrolidone (PVP) were dispersed in ultrapure water. Reg/DMX stock solution was added dropwise under magnetic stirring. The mixture was sonicated with a probe sonicator, dialyzed against deionized water (MWCO, 3.5 kDa) for 24 h, concentrated using a 100-kDa ultrafiltration tube, sterile-filtered (0.22-μm filter), aliquoted, and stored at −20 °C. Reg@BPF NPs and Ce6@BPF NPs were prepared similarly.

Preparation of Cou6@BPF NPs. Cou6 (2 mg) was dissolved in a 1:1 (*v*/*v*) mixture of dichloromethane and ethyl acetate (1 mL total). BPF solution (10 mL) was mixed with olive oil (20 mg), followed by dropwise addition of Cou6 solution. The mixture was vortexed for emulsification and sonicated for 5 min. Organic solvents were removed by rotary evaporation, and the product was sterile-filtered (0.22-μm filter), aliquoted, and cryopreserved.

Interactions between Reg, DMX, and the BPF nanocarrier were examined by FTIR. Hydrodynamic diameter and zeta potential were measured by dynamic light scattering (DLS). Morphology was visualized by transmission electron microscopy (TEM) after negative staining with 2% phosphotungstic acid. X-ray diffraction (XRD) assessed crystalline changes in BPF, Reg, and DMX after nanoparticle formation. Drug loading (DL%) and encapsulation efficiency (EE%) were calculated by UV−vis spectroscopy, using absorbance at 263 nm for Reg and 338 nm for DMX.

2.5. In vitro drug release

In vitro release of Reg and DMX from Reg/DMX@BPF NPs was evaluated by dynamic dialysis under a pH gradient to mimic physiological (pH 7.4 PBS with 1% *w*/*v* PVP), tumor (pH 6.5 acetate buffer with 1% *w*/*v* PVP), and lysosomal (pH 5.5 acetate buffer with 1% *w*/*v* PVP) conditions. Nanoparticles equivalent to 1.0 mg/mL Reg and 0.4 mg/mL DMX were loaded into a dialysis bag (MWCO, 3.5 kDa) and immersed in 50 mL of prewarmed release medium (37 ± 0.5 °C) in an incubator shaker at 100 rpm. At 1, 2, 4, 8, 12, 24, 48, and 72 h, 1 mL of release medium was withdrawn and replaced with an equal volume of fresh, prewarmed medium. Samples were centrifuged, and the supernatant was filtered through a 0.22-μm membrane. The concentrations of Reg and DMX were quantified by UV−vis spectroscopy at 263 and 338 nm, respectively.

2.6. Cellular uptake and lysosomal escape

Cellular uptake. CT26-luc cells, HUVECs, and BMDMs were seeded in 12-well plates and allowed to adhere. The complete medium was replaced with serum-free medium containing free Ce6, Ce6@BSA NPs, Ce6@BPF NPs, or Ce6@BPF NPs preincubated with FA/PBA. To specifically validate the role of FRα in the cellular internalization of BPF nanoparticles, an additional antibody blockade experiment was performed on CT26-luc cells. Cells were pre-treated with folate receptor 1 (FOLR1) antibody at a predetermined concentration for 30 min. Following washing, the cells were then incubated with Ce6@BSA NPs or Ce6@BPF NPs in serum-free medium. Uptake was quantified by flow cytometry, with untreated cells as the negative control. Mean fluorescence intensity (MFI) was recorded for each group.

Spheroid penetration. CT26-luc multicellular spheroids were formed using a 3D cell culture coating kit. Briefly, CT26-luc cells were seeded in U-bottom 96-well plates precoated with the 3D culture coating reagent and incubated at 37 °C for 3 days. Compact and homogeneous spheroids were utilized for penetration studies. Spheroids were treated with Cou6@BSA NPs, Cou6@BPF NPs, or Ce6@BPF NPs preincubated with FA/PBA for 1, 4, or 12 h. They were washed three times with PBS and imaged by confocal microscopy.

Lysosomal escape. BMDMs were incubated with Cou6@BSA NPs or Cou6@BPF NPs for 2, 4, or 8 h, then stained with LysoTracker and Hoechst 33342. After washing, cells were imaged by high-resolution confocal microscopy. Lysosomal colocalization was quantified by Pearson's correlation coefficient (PCC) in cytoplasmic regions (nuclei excluded), using image analysis software. ^{1}H NMR spectra were carried out to compare chemical shifts between PBA and SA. Lysosomal membrane permeabilization was assessed in BMDMs treated with PBS, BSA, BPF, or BPF + SA. Cells were stained with acridine orange (5 μg/mL; 20 min at 37 °C in the dark), washed with PBS, detached, and analyzed by flow cytometry (APC channel). Reduced MFI relative to untreated controls indicated permeabilization.

2.7. Cell proliferation assays and live/dead cell staining

Cell viability was assessed using the Cell Counting Kit-8 (CCK-8) assay. Briefly, CT26-luc cells and HUVECs were seeded in 96-well plates. After 24 h of pre-culture, cells were treated with a gradient concentration of Reg (0−30 μmol/L) for 24, 48, or 72 h. In a separate experiment, CT26-luc cells, HUVECs, and HaCaTs

were seeded and, following a 24-h incubation, treated with serial concentrations of the BPF nanocarrier for 48 h. Moreover, BMDMs and BMDCs were also treated with Reg@BPF NPs for 48 h. Following treatment, 10 μL of CCK-8 reagent was added to each well, and plates were incubated for 2 h in the dark. Absorbance at 450 nm was measured using a microplate reader. Cell viability was calculated as Eq. (1):

$$\text{Cell viability} = (\text{absorbance of treated cells/absorbance of control cells}) \times 100\% \quad (1)$$

Cell death was visualized by live/dead staining. CT26-luc cells were seeded in U-bottom 96-well plates pre-coated with the 3D culture matrix and cultured for 3 days. Compact and homogeneous spheroids were treated with Reg@BPF NPs (5, 7.5, or 10 μmol/L) for 24 h. HUVECs were seeded in confocal dishes (2×10^5cells/dish) and cultured for 24 h. After treatment with Reg@BPF NPs (5, 7.5, or 10 μmol/L) for 24 h, cells were washed with PBS and stained with calcein AM (green fluorescence, for live cells) and propidium iodide (PI, red fluorescence, for dead cells) in PBS for 15−30 min at room temperature (RT) in the dark. After washing, images were acquired using a confocal laser scanning microscope.

2.8. Cell apoptosis and cycle assays

Apoptosis assay. CT26-luc cells were treated with either free Reg (5, 7.5, or 10 μmol/L) or Reg@BPF NPs (5, 7.5, or 10 μmol/L) for 24 h, using PBS as a control. HUVECs were treated with Reg@BPF NPs (5, 7.5, or 10 μmol/L) for 24 h. Following treatment, cells were trypsinized, collected, and washed with PBS. The cell pellets were resuspended in 195 μL of Annexin V binding buffer and stained with 5 μL of Annexin V-FITC for 10 min in the dark. Subsequently, 10 μL of propidium iodide (PI) solution was added, and the samples were incubated for an additional 10 min in the dark. Apoptotic cells were quantified immediately using flow cytometry.

Cell cycle analysis. CT26-luc cells and HUVECs were treated with Reg@BPF NPs (5, 7.5, or 10 μmol/L) for 24 h. After treatment, cells were harvested, resuspended in 300 μL of ice-cold PBS, and fixed by dropwise addition of 700 μL of ice-cold anhydrous ethanol while vortexing. Fixed cells were stored overnight at 4 °C, then centrifuged and washed twice with PBS. Cells were resuspended in 500 μL of PI staining solution containing 50 μg/mL PI and 100 μg/mL RNase A, followed by incubation for 30 min at RT in the dark. Cell cycle distribution across the G0/G1, S, and G2/M phases was determined based on PI fluorescence using flow cytometry.

2.9. Angiogenesis assay

HUVECs were seeded in Matrigel-precoated 12-well plates and divided into five groups: (i) PBS control, or conditioned medium (CM) derived from IL-4 polarized BMDMs that was (ii) untreated or (iii−v) co-treated with Reg@BPF NPs at 5, 7.5, or 10 μmol/L. Following a 12-h incubation, cells were stained with Calcein-AM for 20 min at RT and imaged using an inverted fluorescence microscope equipped with an FITC filter. Three random fields per well were captured for analysis. Tubular junction and mesh numbers were subsequently quantified using the Angiogenesis Analyzer plugin in ImageJ software.

2.10. Assessment of BMDMs polarization and BMDCs maturation

The polarization state of BMDMs was evaluated under different treatment conditions. In the drug treatment experiment, BMDMs were divided into six groups: (i) PBS, (ii) free Reg, (iii) free DMX, (iv) free Reg/DMX combination, (v) Reg@BPF NPs, and (vi) Reg/DMX@BPF NPs. To specifically assess the immunomodulatory effect of the nanocarrier itself, a separate experiment was performed where BMDMs were treated with (i) PBS, (ii) BSA, (iii) BPF, or (iv) free FA/PBA. The maturation of BMDCs was examined under nine conditions: (i) PBS, (ii) free Reg, (iii) free DMX, (iv) free Reg/DMX, (v) Reg@BPF NPs, (vi) Reg/DMX@BPF NPs, (vii) BSA, (viii) BPF, and (ix) free FA/PBA.

For both assays, cells were treated for 24 h, harvested, and analyzed by flow cytometry. BMDMs were stained for the surface markers F4/80, CD86, and CD206, while BMDCs were stained for CD11c, CD80, and CD86. Furthermore, the concentrations of the pro-inflammatory cytokines TNF-α and IL-6 in the culture supernatants were quantified using enzyme-linked immunosorbent assay (ELISA).

2.11. Western blot analysis

Western blot analysis was performed as previously described with modifications. In brief, whole-cell lysates were prepared in RIPA lysis buffer containing protease and phosphatase inhibitors. Protein concentrations were determined using a bicinchoninic acid (BCA) assay. Equal amounts of protein were separated by 10% SDS-polyacrylamide gel electrophoresis (SDS-PAGE) and transferred onto polyvinylidene difluoride (PVDF) membranes. The membranes were blocked and then incubated with specific primary antibodies overnight at 4 °C, followed by incubation with appropriate horseradish peroxidase (HRP)-conjugated secondary antibodies. Protein bands were visualized using an enhanced chemiluminescence (ECL) substrate and imaged with a chemiluminescence detection system.

For specific signaling pathway analyses: (i) To assess VEGFR2 signaling, HUVECs were treated with Reg@BPF NPs (0.5, 1, or 2 μmol/L) for 24 h, and blots were probed with antibodies against VEGFR2 and phosphorylated VEGFR2 (*p*-VEGFR2). (ii) To evaluate the TLR4−NF-κB pathway, BMDMs were treated with BSA, BPF, or a free FA/PBA mixture, and IκB-α levels were detected. (iii) To examine the STING pathway, BMDMs were treated with DMX (5, 10, or 15 μmol/L), and blots were probed with antibodies against cGAS, total STING, and phosphorylated STING (p-STING).

2.12. Immunofluorescence detection of NF-κB p65 nuclear translocation

BMDMs were seeded on sterile glass coverslips and pre-stimulated with IL-4 for 24 h to induce M2 polarization. Cells were then treated with PBS, BSA, BPF, or free FA/PBA for 1 h. Cells were fixed for 15 min at RT, washed three times with PBS, and blocked for 1 h at RT. For immunostaining, cells were incubated overnight at 4 °C with a mouse anti-NF-κB p65 monoclonal antibody. After washing, a Cy3-conjugated anti-mouse secondary antibody was applied and incubated for 1 h at RT in the dark. Nuclei were counterstained with DAPI for 5 min at RT. After final washes, coverslips were mounted with antifade medium.

Fluorescence images were acquired using a fluorescence/confocal microscope (Cy3 channel for p65; DAPI channel for nuclei).

2.13. *In vivo distribution and tumor penetration*

The expression of FRα in major organs and peritoneal tumor tissues was assessed by immunofluorescence staining. Tissue sections were stained with a FOLR1 rabbit polyclonal antibody followed by a Cy3-conjugated secondary antibody, counterstained with DAPI, and imaged using a confocal microscope.

Tumor-bearing mice were randomized into three groups ($n = 4$): free Ce6, Ce6@BSA NPs, and Ce6@BPF NPs. Each mouse received an intraperitoneal injection of Ce6 (5 mg/kg). Real-time biodistribution was monitored at 2, 4, 8, 12, 24, and 48 h using an IVIS Spectrum *in vivo* imaging system. In a separate terminal study, mice were euthanized 12 h after dosing. The heart, liver, spleen, lungs, kidneys, and intestinal tract were excised, gently rinsed, and imaged *ex vivo* for fluorescence.

Tumor penetration was assessed *ex vivo* using metastatic nodules of uniform size from tumor-bearing mice ($n = 3$). Nodules were incubated at 37 °C for 12 h in serum-free medium containing free Ce6, Ce6@BSA NPs, or Ce6@BPF NPs (Ce6, 12.5 μg/mL). Tissues were partially lysed, sonicated, and centrifuged. Supernatants were collected, and Ce6 fluorescence was measured by spectrophotometry (excitation, 625 nm; emission, 668 nm).

2.14. *Evaluation of the antitumor effect of Reg/DMX@BPF NPs in vivo*

Female BALB/c mice were acclimatized for 1 week and injected intraperitoneally with 3×10^5 CT26-luc cells per mouse. Tumor engraftment was confirmed on Day 4 by *in vivo* bioluminescence imaging under isoflurane anesthesia. Mice were randomized into six groups ($n = 10$) based on tumor signal and treated with PBS, BPF (50 mg/kg), free Reg (10 mg/kg), Reg@BSA NPs (10 mg/kg Reg), Reg@BPF NPs (10 mg/kg Reg) or Reg/DMX@BPF NPs (10 mg/kg Reg; 4 mg/kg DMX). Treatments were administered intraperitoneally every other day for four doses. Body weight, clinical signs, and survival were monitored daily.

On Day 14, metastatic burden was assessed by bioluminescence imaging. Blood was collected for serum biochemistry. Primary tumors and major organs (liver, spleen, and kidney) were excised, weighed, and either fixed in 4% paraformaldehyde for histology or processed for further analysis. The entire intestinal tract was examined and photographed to document peritoneal tumor distribution. The remaining six mice per group were maintained for survival observation until Day 50 post-inoculation. Any mouse exhibiting severe ascites, significant body weight loss (>20%), or other humane endpoints was euthanized promptly.

On Day 50, all surviving mice from the Reg/DMX@BPF NPs group were euthanized. Major organs (heart, liver, spleen, lung, kidney, and colon) were collected from long-term survivors, fixed in 4% PFA, and processed for H&E staining to assess potential long-term toxicity. Serum samples obtained on Day 14 were analyzed for aspartate aminotransferase (AST), alanine aminotransferase (ALT), and urea levels using standard commercial kits.

2.15. *Treatment and analysis of the anti-tumor mechanism in a PMC model*

On Day 8 after inoculation, tumor-bearing mice were randomized into six groups ($n = 4$ per group) and treated with PBS, BPF, free Reg, free DMX, Reg@BPF NPs, or Reg/DMX@BPF NPs on Days 8, 10, and 12. On Day 14, blood was collected for serum isolation. The levels of TNF-α and IL-6 in serum were quantified using ELISA kits according to the manufacturer's instructions. The intestinal tract was excised and photographed to document metastatic dissemination, and tumor nodules were collected and weighed. For histopathological evaluation, tumor tissues were fixed in 4% paraformaldehyde, embedded in paraffin, and sectioned.

Immunofluorescence staining was performed to assess blood vessels using antibodies against CD31 and α-smooth muscle actin (αSMA), M2 TAMs using an anti-CD206 antibody, and tumor-infiltrating $CD8^+$ T cells using anti-CD3 and anti-CD8 antibodies. For flow cytometric analysis, single-cell suspensions were prepared from harvested tumor tissues and spleens. Tumor-infiltrating immune cells were stained for surface markers, including CD45, F4/80, and CD86, to identify $CD86^+$ TAMs. Splenocytes were stained for CD45, CD11c, CD80, and CD86 to evaluate the maturation of DCs ($CD80^+CD86^+$ DCs). All samples were analyzed using a flow cytometer, and data were processed with NovoExpress software.

2.16. *Statistical analysis*

All data are presented as mean ± standard deviation (SD). Statistical analyses were performed using GraphPad Prism (Version 10.1.2). For comparisons between two groups, a two-tailed unpaired Student's *t*-test was applied. When comparing three or more groups, one-way analysis of variance (ANOVA) was used, followed by Bonferroni's *post hoc* test for pairwise comparisons where ANOVA indicated a significant difference. Survival data were analyzed by the Kaplan−Meier method, and differences between groups were assessed with the log-rank (Mantel-Cox) test. All experiments included at least three independent biological replicates ($n \geq 3$). Significance levels are denoted as $^*P < 0.05$, $^{**}P < 0.01$, $^{***}P < 0.001$ and $^{****}P < 0.0001$.

3. Results

3.1. *Synthesis and structural characterization of BSA-PBA-FA (BPF) nanocarrier*

The BPF nanocarrier was synthesized by covalently conjugating PBA and FA to the amino groups of BSA using EDCI and NHS chemistry (Supporting Information Fig. S1A). Specifically, the carboxyl groups on PBA and FA were activated as NHS esters, which subsequently reacted with lysine residues of BSA through nucleophilic substitution to form stable amide bonds. Unreacted reagents were removed by dialysis, insoluble particles were filtered through a 0.8-μm membrane, and the purified BPF nanocarrier was lyophilized and stored at −20 °C until further use.

To confirm successful conjugation, FTIR spectroscopy revealed enhanced amide I and II bands at 1650 and 1530 cm^{-1} in BPF compared to native BSA, confirming successful amide bond formation (Fig. S1C). ^1H NMR displayed characteristic aromatic proton signals from FA and PBA at δ 7.20, 7.81, and 7.93 ppm, further validating conjugation (Fig. S1B). UV−Vis spectroscopy showed increased absorbance at 280 nm for BPF, attributed to the $\pi-\pi^*$ transition of FA's conjugated aromatic system (Fig. 2A). The functionality of PBA was confirmed using the Alizarin Red S (ARS) assay, which exhibited a 43 nm bathochromic shift,

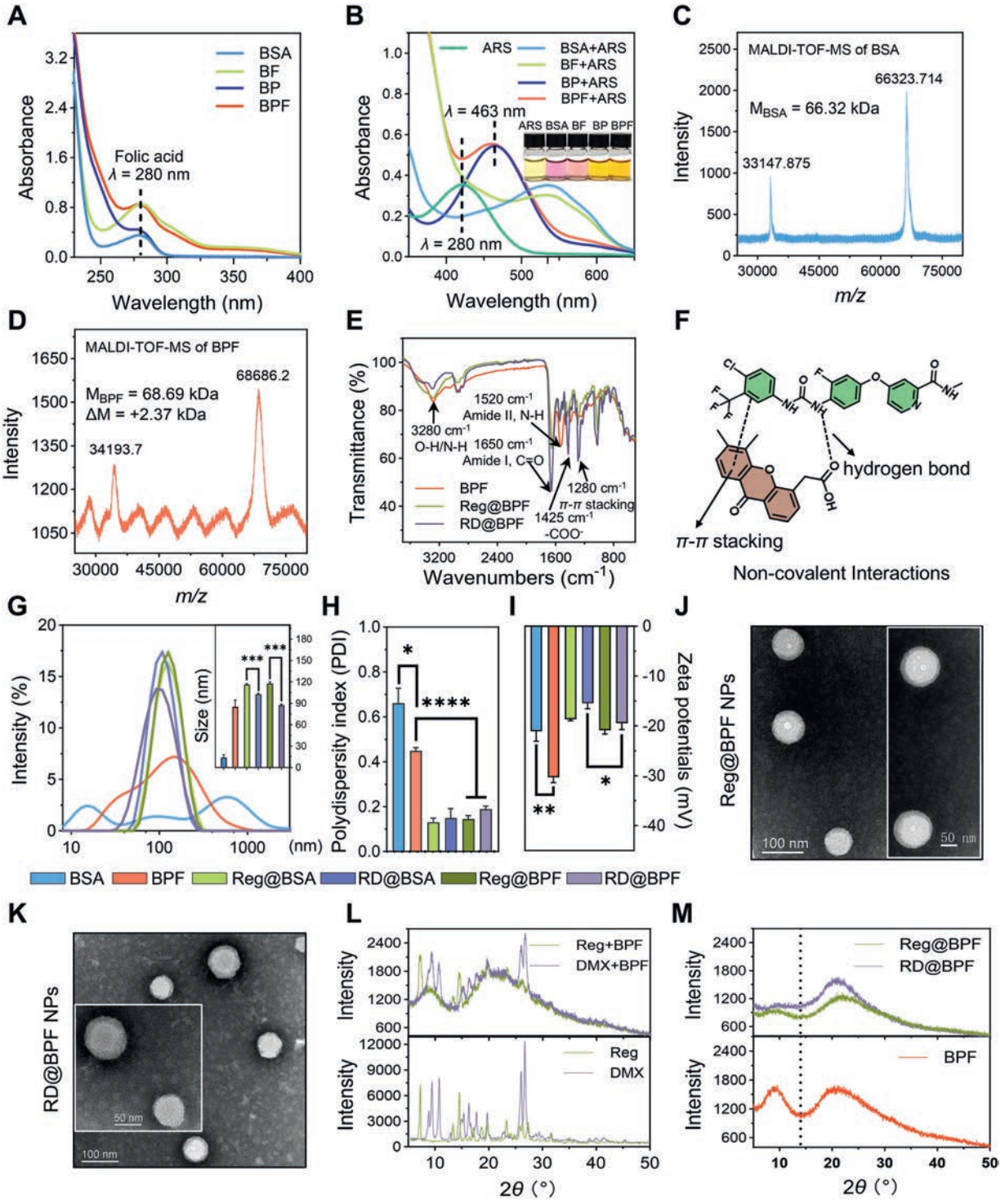

Figure 2 Preparation and characterization of BPF nanocarrier and Reg/DMX@BPF NPs. (A) UV−Vis absorption spectra of BSA, BSA-FA (BF, folic acid (FA)), BSA-PBA (BP), and BSA-PBA-FA (BPF). (B) UV−Vis spectra of ARS and co-incubated with BSA, BF, BP, and BPF. (C, D) MALDI-TOF-MS analysis of BSA and BPF. (E) FTIR spectra of BPF, Reg@BPF NPs, and Reg/DMX@BPF NPs. (F) Schematic illustration of the non-covalent interactions between Regorafenib (Reg) and DMXAA (DMX). (G−I) Hydrodynamic diameter, PDI, and zeta potential of various nanoparticle formulations ($n = 3$). (J, K) TEM images of Reg@BPF NPs and Reg/DMX@BPF NPs. (L, M) XRD patterns of BPF, free Reg/DMX, Reg@BPF NPs, and Reg/DMX@BPF NPs. The data are expressed as means ± SD. *$P < 0.05$, **$P < 0.01$, ***$P < 0.001$, ****$P < 0.0001$. RD = Reg/DMX.

indicative of covalent boronate ester formation between the trigonal planar $B(OH)_2$ of PBA and ARS's *ortho*-dihydroxy groups (Fig. 2B). In contrast, native BSA induced a distinct 535 nm red shift due to non-specific hydrophobic interactions.

ICP-MS quantified a sulfur-to-boron molar ratio of 455.55:73.78 (S: B = 6.17) in BPF (Supporting Information Tables S1 and S2). Given that BSA contains 35 sulfur atoms per molecule, this ratio corresponds to approximately 5.7 PBA molecules conjugated per BSA. Molecular weight analysis *via* matrix-assisted laser desorption ionization time-of-flight mass spectrometry (MALDI-TOF-MS) revealed an increase from 66.32 kDa for native BSA to 68.69 kDa for BPF ($\Delta M = +2.37$ kDa), consistent with the addition of PBA and FA (Fig. 2C and D). Based on FA's molecular weight (441.4 Da), this mass shift indicates conjugation of approximately 3.6 FA molecules per BSA molecule.

3.2. Preparation and characterization of Reg/DMX@BPF NPs

BPF-based nanoparticles were prepared by controlled nanoprecipitation. However, DMX alone caused immediate turbidity, due to its planar aromatic structure and acidic group, which induced rapid hydrophobic aggregation and partial unfolding of the protein carrier. Notably, co-loading with Reg prevented precipitation and promoted the formation of Reg/DMX@BPF NPs (Fig. S1E and S1F). FTIR analysis provided mechanistic insights (Fig. 2E). Enhanced intensity at 1425 cm^{-1} (symmetric $-COO^-$ stretch) in Reg/DMX@BPF NPs indicated ionization and encapsulation of DMX's carboxylic acid group within the protein matrix. Attenuation of the amide II band (1520 cm^{-1}, N−H bending) suggested that Reg primarily bound to BPF's hydrophobic sites *via* hydrogen bonding and $\pi-\pi$ stacking, shielding these domains from disruptive interactions with DMX. Furthermore, the emergence of a peak at 1280 cm^{-1} (attributed to $\pi-\pi$ stacking or C−O/C−F vibrations) supported cooperative aromatic interactions between Reg's fluorophenyl/urea moieties and DMX's xanthenone ring. These bindings induced subtle conformational adjustments in BPF, evidenced by increased amide I intensity at 1650 cm^{-1}(C═O stretch), potentially reflecting enhanced α-helical ordering or reduced random coil content. Collectively, Reg acts as a molecular scaffold to facilitate ordered incorporation of DMX *via* synergistic non-covalent interactions (Fig. 2F).

We next examined the physicochemical properties of the BPF nanocarrier and drug-loaded nanoparticles. DLS revealed that BPF had a hydrodynamic diameter of 84.9 ± 9.6 nm, markedly larger than unmodified BSA (14.1 ± 3.8 nm) (Fig. 2G). Although BPF exhibited a lower polydispersity index (PDI) compared to BSA (0.45 ± 0.01 *vs.* 0.63 ± 0.10), its size distribution remained relatively broad (Fig. 2H). Upon drug loading, the nanoparticles displayed uniform sizes with PDI <0.2 (Fig. 2H). Importantly, Reg/DMX@BPF NPs were smaller than Reg@BPF NPs (87.3 ± 1.7 nm *vs.* 117.5 ± 2.5 nm), a trend also observed with BSA groups (Fig. 2G), which may enhance nanoparticle uptake and penetration. Moreover, stability test confirmed that Reg/DMX@BPF NPs maintained stable hydrodynamic diameter and PDI in physiological medium (PBS containing 4% BSA) over 72 h, demonstrating favorable colloidal stability (Fig. S1I−S1K). Surface charge analysis showed that BPF nanocarrier carried a stronger negative potential than BSA, which was preserved after drug loading (−20.9 ± 0.8 mV for Reg/DMX@BPF NPs *vs.* −15.4 ± 1.1 mV for Reg/DMX@BSA NPs) (Fig. 2I). TEM confirmed the amorphous morphology of BPF nanocarrier (Fig. S1D). Reg@BPF NPs showed a core−shell structure, while Reg/DMX@BPF NPs formed amorphous spheres, consistent with their smaller size observed by DLS (Fig. 2J and K).

XRD analysis supported these findings (Fig. 2L and M). Physical mixtures of drugs with BPF retained sharp crystalline peaks of Reg and DMX (5−30°), whereas these disappeared in Reg@BPF NPs and Reg/DMX@BPF NPs, confirming molecular-level dispersion in an amorphous state. Moreover, a reduced intensity of the broad BPF peak (5−14°) indicated that drug incorporation disrupted the protein matrix ordering. For Reg@BPF NPs, diminished peak intensity in the 14−30° range suggested a phase-separated core-shell structure. In contrast, Reg/DMX @BPF NPs exhibited uniform scattering, consistent with their amorphous dispersion.

The encapsulation efficiency (EE%) and drug loading (DL%) of Reg/DMX@BPF NPs reached impressive levels of 77.57 ± 1.20% and 7.60 ± 0.10% for Reg, and 64.30 ± 1.45% and 3.03 ± 0.12% for DMX, respectively. *In vitro* release studies revealed pH-responsive kinetics (Fig. S1G and S1H). At physiological conditions (pH 7.4), both Reg and DMX were released in a sustained manner, with 45.76 ± 4.32% and 46.12 ± 2.99% released after 48 h, respectively. In acidic conditions (pH 6.5), mimicking the TME, release rates increased significantly to 56.57 ± 3.59% for Reg and 62.13 ± 4.34% for DMX after 48 h, highlighting the potential for drug release in the tumor. Notably, drug release was most pronounced at the more acidic lysosomal pH 5.5, with cumulative releases reaching 68.78 ± 3.21% for Reg and 72.98 ± 4.33% for DMX after 48 h, underscoring the critical role of the endocytic acidification gradient in triggering intracellular drug release.

3.3. Cellular uptake and lysosomal escape of BPF-based nanoparticles

To exploit the overexpression of FRα and SA in tumor tissues, we designed a BSA nanocarrier functionalized with FA and PBA, thereby enhancing endocytosis and lysosomal escape (Fig. 3A). Flow cytometry demonstrated that Ce6@BPF NPs were internalized far more efficiently than free Ce6 or Ce6@BSA NPs across CT26-luc cells, HUVECs, and BMDMs (Fig. 3B−G). Uptake was minimal for free Ce6 in CT26-luc cells but modestly higher in BMDMs, reflecting their innate phagocytic activity. Nevertheless, even in BMDMs, Ce6@BPF NPs achieved substantially higher accumulation than Ce6@BSA NPs. Importantly, pre-treatment with excess FA and PBA or FRα-specific antibody blockade markedly reduced Ce6@BPF NPs uptake (Supporting Information Fig. S2A and S2B), confirming that FA and PBA functionalization mediates specific interactions that drive nanoparticle internalization.

Building on efficient uptake, we next examined whether this advantage translated into improved tumor penetration. In 3D CT26-luc spheroids, confocal imaging revealed a time-dependent accumulation of Cou6-labeled nanoparticles over 1, 4, and 12 h (Fig. 3H−J). By 12 h, Cou6@BPF NPs penetrated nearly the entire spheroid, whereas Cou6@BSA NPs remained largely confined to the periphery. Preincubation with FA/PBA sharply attenuated this penetration, underscoring the critical contribution of dual ligand recognition to both cellular uptake and intercellular transport. Quantitative analysis (Fig. 3K) highlighted the superior performance of the BPF nanocarrier, suggesting that its design not only improves initial cell binding but also enables deep tissue diffusion.

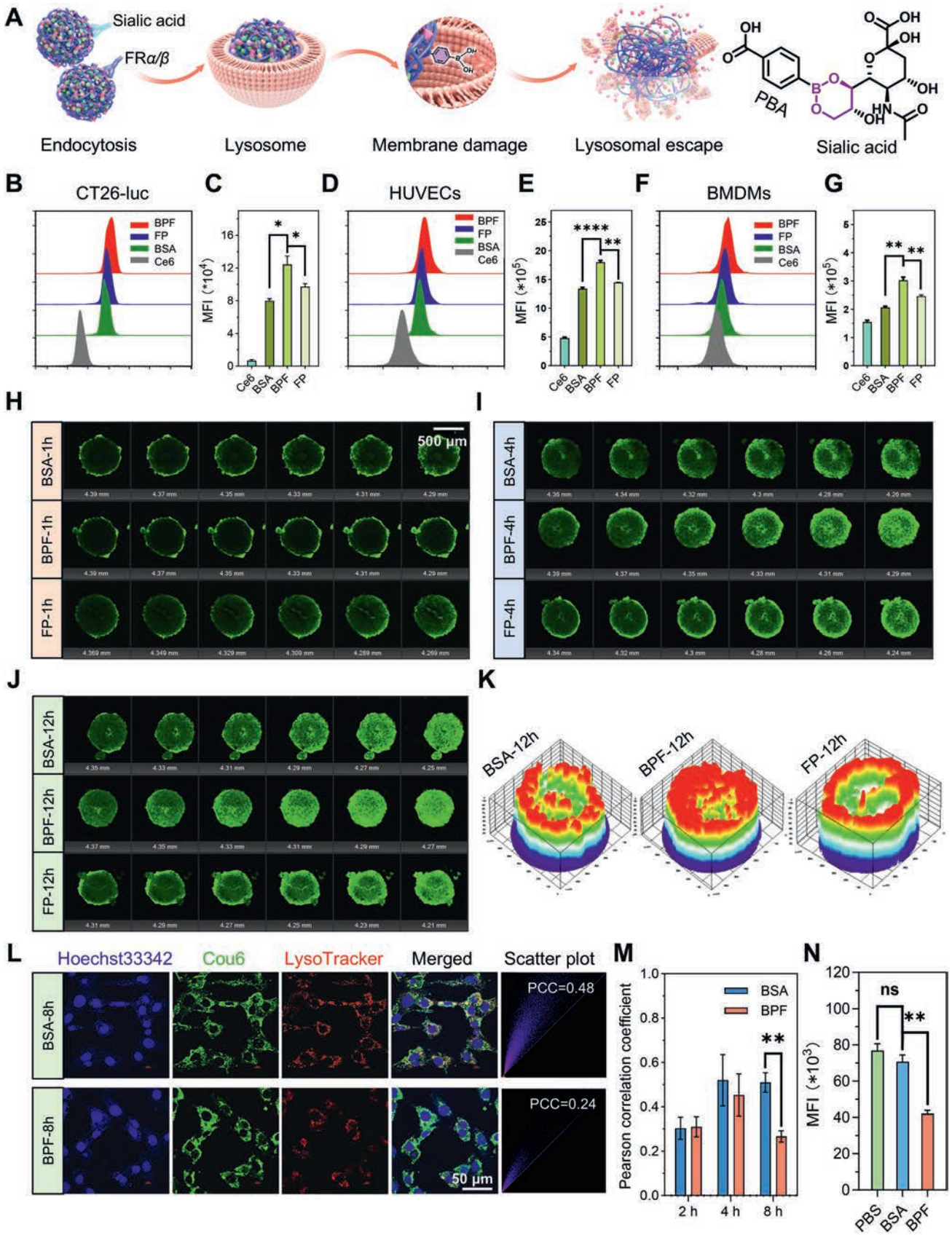

Figure 3 Cellular uptake, penetration, and lysosomal escape of nanoparticles. (A) Schematic of the nanoparticles' endocytosis and lysosomal escape mechanisms. (B−G) Flow cytometry analysis of cellular uptake of nanoparticles in CT26-luc cells, HUVECs, and BMDMs, with MFI quantification ($n = 3$). (H−J) Penetration of Cou6@BSA NPs, Cou6@BPF NPs, and Cou6@BPF NPs preincubated with FA/PBA in CT26-luc

Efficient intracellular delivery further requires escape from lysosomal destabilization. Co-localization analysis using Pearson's correlation coefficient (PCC) revealed distinct behaviors between the nanocarriers over time (Fig. 3L, Fig. S2C). A time-kinetic study at 2, 4, and 8 h showed that Cou6@BSA NPs exhibited high and sustained lysosomal entrapment, with PCC values of 0.30 ± 0.05, 0.52 ± 0.12, and 0.51 ± 0.04, respectively, indicating ineffective escape. In contrast, Cou6@BPF NPs displayed partial co-localization at 2 h (0.31 ± 0.05) and 4 h (0.45 ± 0.10), followed by a significant decrease to 0.27 ± 0.03 at 8 h (Fig. 3M). This dynamic shift demonstrates that BPF-based nanoparticles escape lysosomal degradation over time, transitioning from early lysosomal capture to effective cytoplasmic redistribution.

Mechanistically, this lysosomal escape was attributed to the PBA-induced destabilization of lysosomal membranes. The underlying mechanism involves the specific interaction between PBA and SA residues, which are enriched on glycosylated lysosomal membrane proteins. ^{1}H NMR confirmed the formation of boronate ester bonds between PBA and SA (Fig. S2D). A decrease in the fluorescence signal of Acridine orange (AO) in the APC channel can indicate an increase in lysosomal membrane permeability. The results revealed marked loss of lysosomal integrity in BPF-treated BMDMs, with significantly reduced fluorescence compared to BSA-treated or control cells (Fig. 3N). Crucially, this disruptive effect was substantially reversed when the PBA sites on BPF were pre-blocked with free SA, confirming the specificity and necessity of this binding for lysosomal membrane permeabilization (Fig. S2E and S2F). Collectively, these findings demonstrate that the functionalization with FA and PBA enhances tumor-selective uptake, deep tissue penetration, and efficient lysosomal escape, thereby ensuring effective cytosolic delivery of therapeutic cargo.

3.4. In vitro cytotoxicity and biocompatibility

To investigate the anti-proliferative effects of Reg@BPF NPs on colorectal cancer cells, we first assessed their impact on CT26-luc cells' viability using CCK-8 assays. Reg exhibited robust, dose- and time-dependent inhibition of cell proliferation (Fig. 4A). Higher Reg concentrations significantly reduced cell viability at 24, 48, and 72 h, with prolonged exposure at any given dose further decreasing viability, consistent with a cumulative cytotoxic effect. Live/dead staining was performed using a 3D tumor spheroid model to more reliably retain cells and accurately assess cytotoxicity. In this model, Calcein-AM/PI imaging showed a clear, concentration-dependent effect: treatment with Reg@BPF NPs resulted in a progressive loss of Calcein-AM fluorescence (green, live cells) and a concurrent, marked increase in PI fluorescence (red, dead cells) (Fig. 4B, Supporting Information Fig. S3A). This demonstrates significant cell death consistent with the anti-proliferative effects observed in the viability assays.

Mechanistic studies indicated that Reg@BPF NPs induced both apoptosis and G1-phase cell cycle arrest. Quantification of apoptosis by Annexin V/PI staining revealed a dose-dependent increase in total apoptotic cells (early and late), from 10.36 ± 0.26% in the PBS control to 30.04 ± 2.25% at 5 μmol/L, 67.25 ± 1.81% at 7.5 5 μmol/L, and 82.70 ± 1.52% at 10 5 μmol/L (Fig. 4C and D). Notably, the pro-apoptotic effect of Reg@BPF NPs was stronger than that of free Reg at lower concentrations, with apoptosis rates of 30.04 ± 2.25% *versus* 22.07 ± 1.76% at 5 5 μmol/L, and 67.25 ± 1.81% *versus* 54.50 ± 2.85% at 7.5 5 μmol/L (Fig. S3B and S3C). These results underscore a key advantage of the nanocarrier: enhanced therapeutic efficacy at lower doses, which may improve the therapeutic index. Cell cycle analysis confirmed a dose-dependent accumulation in G1 phase with a corresponding reduction in S-phase cells (Fig. 4E and F). The G1 fraction increased from 36.94 ± 0.95% in controls to 50.79 ± 3.48% at 5 μmol/L, 54.20 ± 0.97% at 7.5 μmol/L, and 73.83 ± 2.07% at 10 μmol/L, reflecting a two-fold rise at the highest dose. In parallel, the S-phase fraction decreases by approximately 62.4% relative to controls, indicating that Reg@BPF NPs block S-phase entry or progression. These cell cycle changes align with Reg's known inhibition of Raf signaling, providing a mechanistic basis for the observed anti-proliferative effects.

Finally, the BPF nanocarrier displayed excellent *in vitro* biocompatibility. Hemolysis assays showed negligible hemoglobin release for BPF compared to the water positive control (Fig. 4G). Additionally, CCK-8 assays showed minimal cytotoxicity of BPF up to 100 μg/mL in CT26-luc cells, HaCaTs, and HUVECs (Fig. 4H). Critically, Reg@BPF NPs exhibited minimal toxicity toward key immune cells, with viabilities remaining above 85% for both BMDMs and BMDCs even at 10 μmol/L, a concentration that potently inhibited CT26-luc cells' viability (Fig. 4I and J). Together, these data indicate that BPF is a well-tolerated delivery platform and that Reg@BPF NPs exert potent, dose-dependent anti-proliferative effects on CT26-luc cells through apoptosis induction and a pronounced G1 cell-cycle arrest.

3.5. Inhibition of angiogenesis by Reg@BPF NPs

Reg is a clinically approved multi-kinase inhibitor that suppresses angiogenesis by targeting endothelial receptors such as VEGFR2, thereby inhibiting vascular endothelial cell proliferation and migration. CCK-8 assays confirmed that Reg exerted potent proliferation inhibition in a dose- and time-dependent manner, with viability steadily declining as concentration and exposure time increased (Fig. 5A). Live/dead staining further validated this effect, showing extensive cell death at higher Reg@BPF NPs concentrations (Fig. 5B). Flow cytometry revealed that Reg@BPF NPs markedly induced apoptosis in a concentration-dependent manner, rising from 5.03 ± 0.47% in controls to over 40.74 ± 2.91% at 10 μmol/L (Fig. 5C and D). In parallel, Reg@BPF NPs strongly arrested HUVECs in the G1 phase (Fig. 5E and F). The fraction of cells in G1 increased from PBS (39.67 ± 1.42%) to 5 μmol/L (52.33 ± 1.34%) and peaked at 10 μmol/L (85.52 ± 1.74 %), underscoring their ability to block cell-cycle progression. Together, these results indicate that Reg@BPF NPs suppress endothelial proliferation through dual mechanisms of apoptosis induction and G1 arrest.

The functional impact on angiogenesis was further validated using a 3D Matrigel tube formation assay. Conditioned medium from M2 TAMs (M2 CM) significantly promoted endothelial tube

spheroids at 1, 4, and 8 h (scale bar = 500 μm). (K) 3D surface plots quantifying penetration depth in spheroids. (L) Lysosomal colocalization of Cou6@BSA NPs and Cou6@BPF NPs in BMDMs after 8 h (scale bar = 50 μm). (M) Quantification of the PCC at 2, 4, and 8 h (n = 3). (N) MFI quantification of AO in BMDMs (n = 3). The data are expressed as means ± SD. $^{ns}P > 0.05$, $^{*}P < 0.05$, $^{**}P < 0.01$, $^{****}P < 0.0001$. FP = preincubated with FA/PBA.

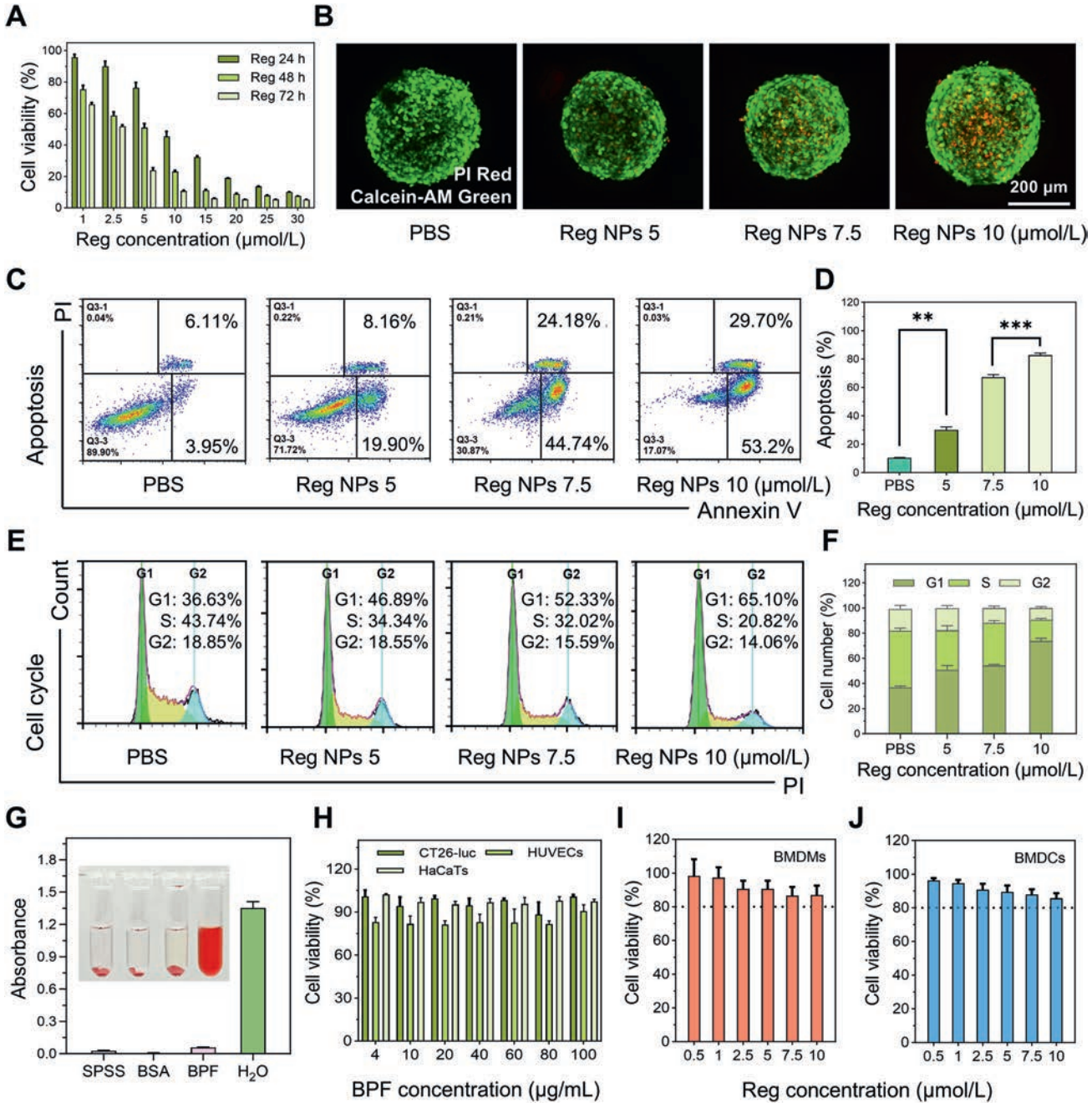

Figure 4 *In vitro* cytotoxicity and biocompatibility. (A) Viability of CT26-luc cells treated with varying concentrations of Reg for 24, 48, and 72 h ($n = 3$). (B) Live/dead cell staining of 3D CT26-luc spheroids (scale bar = 200 μm). (C, D) Flow cytometry analysis of apoptosis in CT26-luc cells ($n = 3$). (E, F) Cell cycle arrest analysis in CT26-luc cells ($n = 3$). (G) Hemolysis assay evaluating the biocompatibility of BPF nanocarrier ($n = 3$). (H) Viability of CT26-luc cells, HaCaTs, and HUVECs treated with BPF ($n = 3$). (I, J) Viability of BMDMs and BMDCs treated with Reg@BPF NPs for 48 h ($n = 3$). The data are expressed as means ± SD. $^{**}P < 0.01$, $^{***}P < 0.001$. Reg NPs = Reg@BPF NPs.

formation, evidenced by higher numbers of junctions and meshes. Remarkably, Reg@BPF NPs effectively counteracted this pro-angiogenic stimulus, dose-dependently reducing both junctions and meshes and nearly abolishing M2 CM-induced network formation at 10 μmol/L (Fig. 5G and H). At the molecular level, Western blotting confirmed that Reg@BPF NPs suppressed VEGFR2 phosphorylation in HUVECs without affecting total VEGFR2, thereby directly blocking a central angiogenic signaling axis (Fig. 5I). A schematic illustration (Fig. 5J) summarizes the mechanism, highlighting how Reg@BPF NPs inhibit VEGFR2-mediated signaling to suppress endothelial proliferation and angiogenesis.

3.6. BMDMs repolarization and BMDCs maturation mediated by Reg/DMX@BPF NPs

To determine whether Reg/DMX@BPF NPs could reprogram immunosuppressive TME, we first examined their effect on

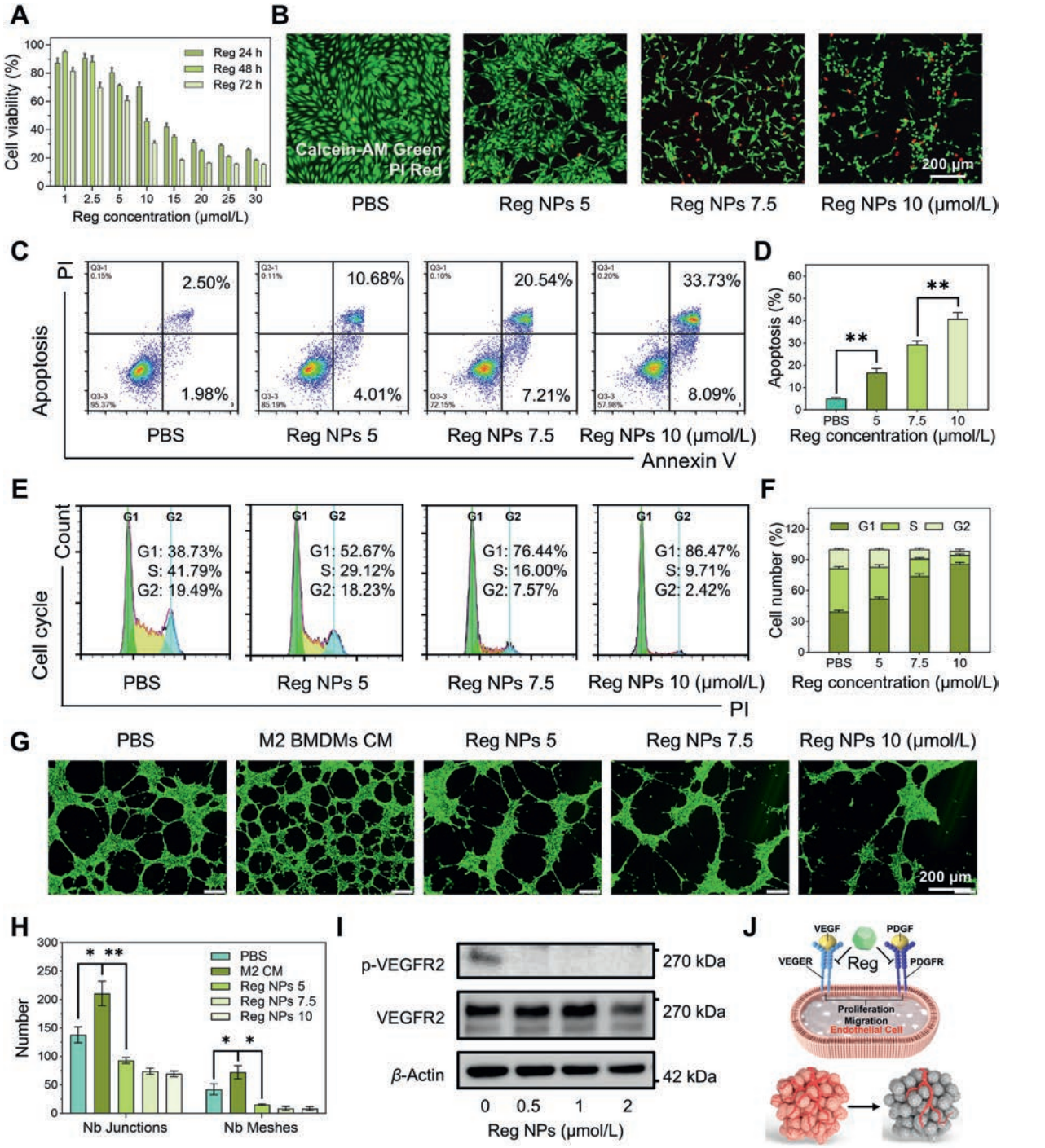

Figure 5 Inhibition of HUVECs proliferation and angiogenesis by Reg@BPF NPs. (A) Viability of HUVECs treated with varying concentrations of Reg for 24, 48, and 72 h ($n = 3$). (B) Live/dead cell staining of HUVECs (scale bar = 200 μm). (C, D) Flow cytometry analysis of apoptosis in HUVECs induced by Reg@BPF NPs ($n = 3$). (E, F) Cell cycle arrest analysis in HUVECs treated with Reg@BPF NPs, with quantification of G1/S/G2 phase distribution ($n = 3$). (G, H) *In vitro* tube formation assay treated with Reg@BPF NPs, with the last four groups treated with the M2 BMDMs conditioned medium (CM) ($n = 3$) (scale bar = 200 μm). (I) Western blot analysis of VEGFR2 phosphorylation levels in HUVECs. (J) Schematic illustrating Reg-mediated inhibition of VEGFR2, HUVECs proliferation, and angiogenesis. The data are expressed as means ± SD. *$P < 0.05$, **$P < 0.01$. Reg NPs = Reg@BPF NPs.

BMDMs. The gating strategies for flow cytometry are detailed in Supporting Information Fig. S4A (BMDMs) and Fig. S4E (BMDCs). The analysis of CD86, a marker of pro-inflammatory M1 macrophages, revealed that free Reg and free DMX individually induced modest polarization (25.21 ± 2.77% and 30.94 ± 2.55%, respectively), compared to only 9.60 ± 3.20% in PBS controls. The Reg/DMX combination further enhanced $CD86^+$ cells to 54.84 ± 1.12% (Fig. 6A and B). Strikingly, BPF-

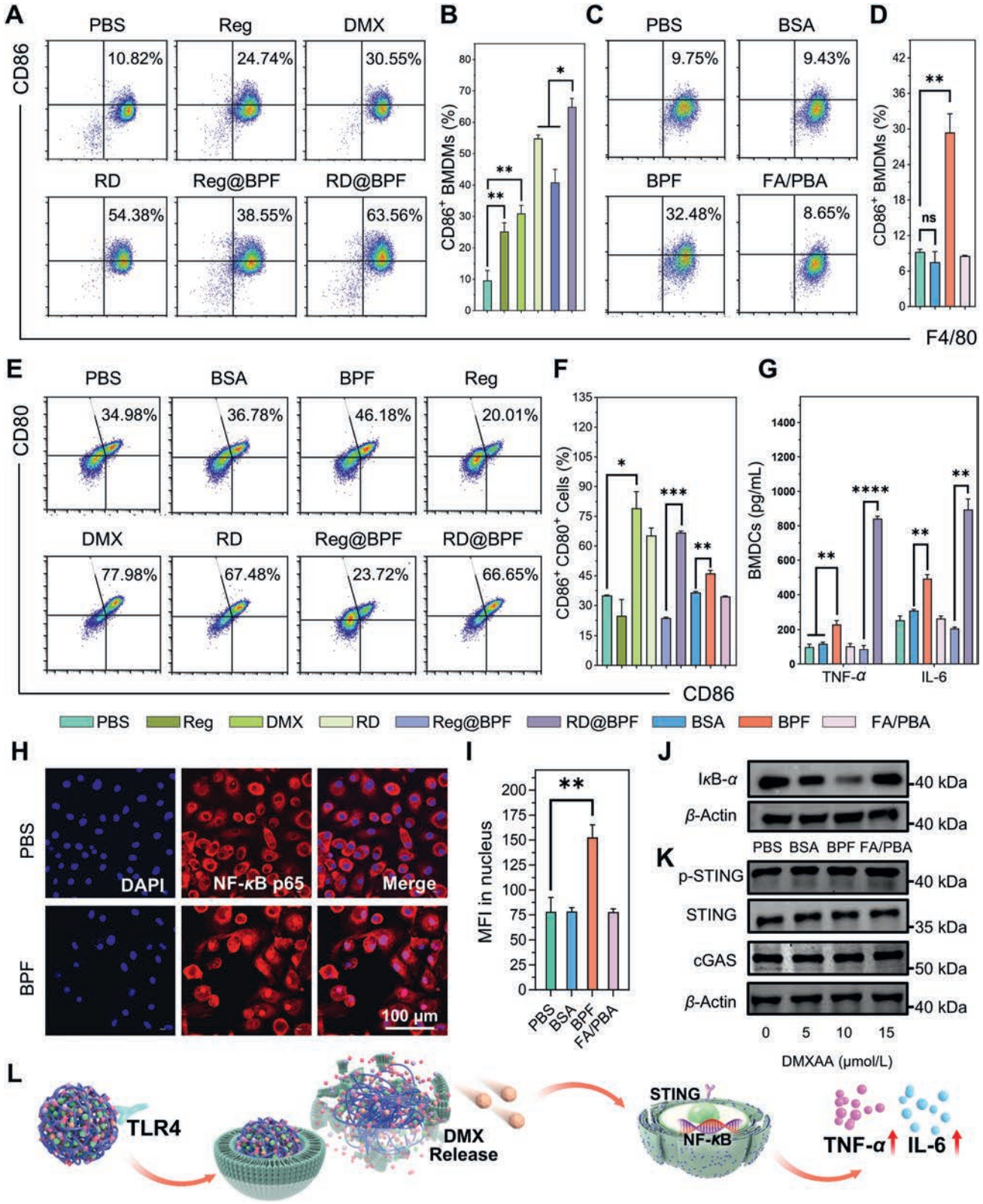

Figure 6 Polarization of BMDMs and maturation of BMDCs. (A−D) Flow cytometry analysis of F4/80 and CD86 expression on BMDMs, with quantification of F4/80^{+}CD86^{+} BMDMs (n = 3). (E, F) Flow cytometry analysis and statistical evaluation of CD80 and CD86 expression on BMDCs (n = 3). (G) Secretion levels of TNF-α and IL-6 in the supernatants of BMDCs (n = 3). (H) Immunofluorescence analysis of NF-κB p65 nuclear translocation in BMDMs (scale bar = 100 μm). (I) Quantification of NF-κB intensity within nuclei of BMDMs (n = 3). (J) Western blot analysis of IκB-α degradation in BMDMs. (K) Western blot analysis of cGAS, STING, and p-STING levels in BMDMs after DMX treatment. (L) Schematic illustration of the immune activation mechanism mediated by DMX and BPF. The data are expressed as means ± SD. *P< 0.05, **P< 0.01, ***P< 0.001, ****P< 0.0001. RD = Reg/DMX.

based formulations achieved even stronger effects. Reg@BPF NPs increased M1 polarization to 40.78 ± 4.25%, significantly higher than free Reg, while Reg/DMX@BPF NPs induced the highest conversion at 64.88 ± 2.72%, clearly surpassing the free drug combination. Concurrently, it potently suppressed the M2 phenotype, reducing the population of $CD206^+$ BMDMs from 60.62 ± 2.07% to 13.87 ± 4.15% (Fig. S4B and S4C). This potent synergy suggested a potential immunomodulatory role for the BPF itself. The contribution of BPF was further validated using control groups. BPF alone significantly upregulated CD86 expression (29.40 ± 3.17%), whereas BSA or FA/PBA had a negligible impact (Fig. 6C and D). This indicates that BPF, likely due to PAMP-like structures on its surface, directly promotes M1 polarization. Consistently, BPF and its drug-loaded variants induced progressive increases in TNF-α and IL-6 secretion from BMDMs, reinforcing their pro-inflammatory phenotype (Fig. S4D).

We next assessed the impact on BMDCs, which are critical for initiating adaptive immunity. DMX treatment alone strongly promoted BMDCs maturation, as evidenced by a high proportion of $CD80^+CD86^+$ cells (79.16 ± 8.28%). In contrast, free Reg markedly suppressed maturation (24.79 ± 8.27%), even below PBS controls (35.05 ± 0.18%), an effect that was largely reversed in the Reg/DMX combination (Fig. 6E and F). Notably, BPF alone significantly enhanced BMDCs' maturation relative to controls, consistent with its activity in BMDMs (Fig. 6F, Fig. S4F). Although Reg@BPF NPs retained partial suppressive effects, Reg/DMX@BPF NPs induced robust BMDCs maturation (66.82 ± 0.74%), closely approximating the efficacy of the free drug combination. These functional changes correlated with elevated secretion of TNF-α and IL-6 in BMDCs supernatants (Fig. 6G).

To explore the underlying mechanism, we examined the TLR4−NF-κB signaling axis. The effect of BPF was significantly attenuated by the TLR4-specific inhibitor, confirming TLR4 involvement in BPF-induced M1 polarization (Fig. S4H and S4I). At the molecular level, in PBS, BSA, and FA/PBA groups, NF-κB p65 largely remained cytoplasmic. By contrast, BPF-treated BMDMs displayed clear nuclear translocation of NF-κB p65, as indicated by intense red fluorescence colocalizing with DAPI-stained nuclei and confirmed by a significant increase in the nuclear fluorescence intensity of p65 (Fig. 6H and I, Fig. S4G). Mechanistically, BPF treatment induced the degradation of IκB-α, a key step in the TLR4−NF-κB axis activation (Fig. 6J). Furthermore, DMX treatment directly activated the STING pathway, as evidenced by increased levels of p-STING without altering total STING or cGAS expression (Fig. 6K). Together, these results support a model in which BPF acts in concert with DMX to activate the TLR4/NF-κB and STING pathway, respectively, driving TAMs repolarization, DCs maturation and secretion of pro-inflammatory cytokines (Fig. 6L).

3.7. In vivo biodistribution and anti-tumor effects of Reg/DMX@BPF NPs

Building on the potent *in vitro* anti-angiogenic and immunomodulatory effects, we assessed the biodistribution and therapeutic efficacy of Reg/DMX@BPF NPs in a PMC model. *In vivo* fluorescence imaging following intraperitoneal administration revealed distinct pharmacokinetic behaviors (Fig. 7A). Although fluorescence intensity decreased over time across all groups, Ce6@BPF NPs maintained the highest fluorescence intensity during early (2−8 h) and mid-term intervals, reflecting prolonged peritoneal retention relative to free Ce6, which dissipated rapidly (Supporting Information Fig. S5A). *Ex vivo* organ imaging 12 h post-injection showed predominant accumulation in the liver and intestines, with minimal uptake in the heart and spleens, aligning with expected biodistribution patterns following intraperitoneal delivery (Fig. 7B). Notably, Ce6@BPF NPs exhibited intense fluorescence in tumor nodules, a finding corroborated by quantitative extraction from tumor lysates, which demonstrated significantly higher Ce6 delivery with Ce6@BPF NPs *versus* Ce6@BSA NPs or free Ce6 (Fig. S5B). Immunofluorescence staining confirmed the overexpression of FRα in peritoneal tumor tissues, providing a solid foundation for active targeting, while also detecting its basal expression in kidneys (Fig. S5E). This enhanced tumor targeting underscores the synergistic benefits of FRα recognition and PBA-SA interactions facilitated by the BPF nanocarrier.

Bioluminescence imaging verified uniform tumor engraftment across groups on day 4 (Fig. 7C). By Day 14, PBS-treated mice exhibited intense abdominal luminescence consistent with aggressive metastatic spread, whereas the Reg/DMX@BPF NPs group showed signal intensity near baseline levels. Necropsy corroborated these findings, revealing extensive peritoneal metastases in controls, characterized by dense nodular coverage across the mesentery and gastrosplenic ligament (Fig. 7D). In contrast, Reg/DMX@BPF NPs nearly eliminated visible tumor metastases. Quantitative tumor burden analysis established a clear efficacy gradient (Fig. 7E). PBS-treated mice bore the heaviest tumor loads (1.55 ± 0.34 g), while free Reg reduced this to 0.94 ± 0.26 g. Reg@BSA NPs further lowered tumor weight to 0.67 ± 0.20 g, and Reg@BPF NPs achieved a robust suppression to 0.45 ± 0.09 g. Reg/DMX@BPF NPs exhibited the most pronounced inhibition, reducing tumor weight to 0.13 ± 0.05 g and representing a 92% reduction *versus* PBS. These results are consistent with bioluminescence trends (Fig. S5C). Strikingly, only Reg/DMX@BPF NPs completely prevented ascites formation (Fig. 7F), a critical clinical marker of uncontrolled carcinomatosis, highlighting their superior therapeutic impact. Importantly, this potent anti-tumor effect translated into a significant survival benefit, as evidenced by Kaplan−Meier analysis (Fig. 7G).

All treatment regimens were well-tolerated, with no significant signs of systemic toxicity. Transient mild body weight loss and diarrhea were observed around Day 10 but resolved spontaneously without intervention (Fig. 7H). Histopathological examination by H&E staining revealed no structural abnormalities in the liver, kidney, or spleen across all groups (Fig. 7I, Fig. S5D). Serum biochemical analyses of hepatic (ALT, AST) and renal (UREA) function remained within normal physiological ranges (Fig. 7J−L), indicating no signs of organ impairment. Long-term safety assessment further confirmed the favorable biosafety profile, as H&E staining of major organs (heart, liver, spleen, lung, kidney, and colon) showed intact tissue architecture with no evidence of pathological injury, inflammatory infiltration, necrosis, or fibrosis (Fig. S5F). Together, these results underscore the robust therapeutic efficacy and excellent systemic safety of Reg/DMX@BPF NPs, supporting their potential as an intraperitoneal theranostic nanoplatform for the treatment of PMC.

3.8. In vivo anti-angiogenic and immunotherapeutic effects of Reg/DMX@BPF NPs

To evaluate the therapeutic efficacy of Reg/DMX@BPF NPs in advanced disease, we delayed treatment initiation until Day 8

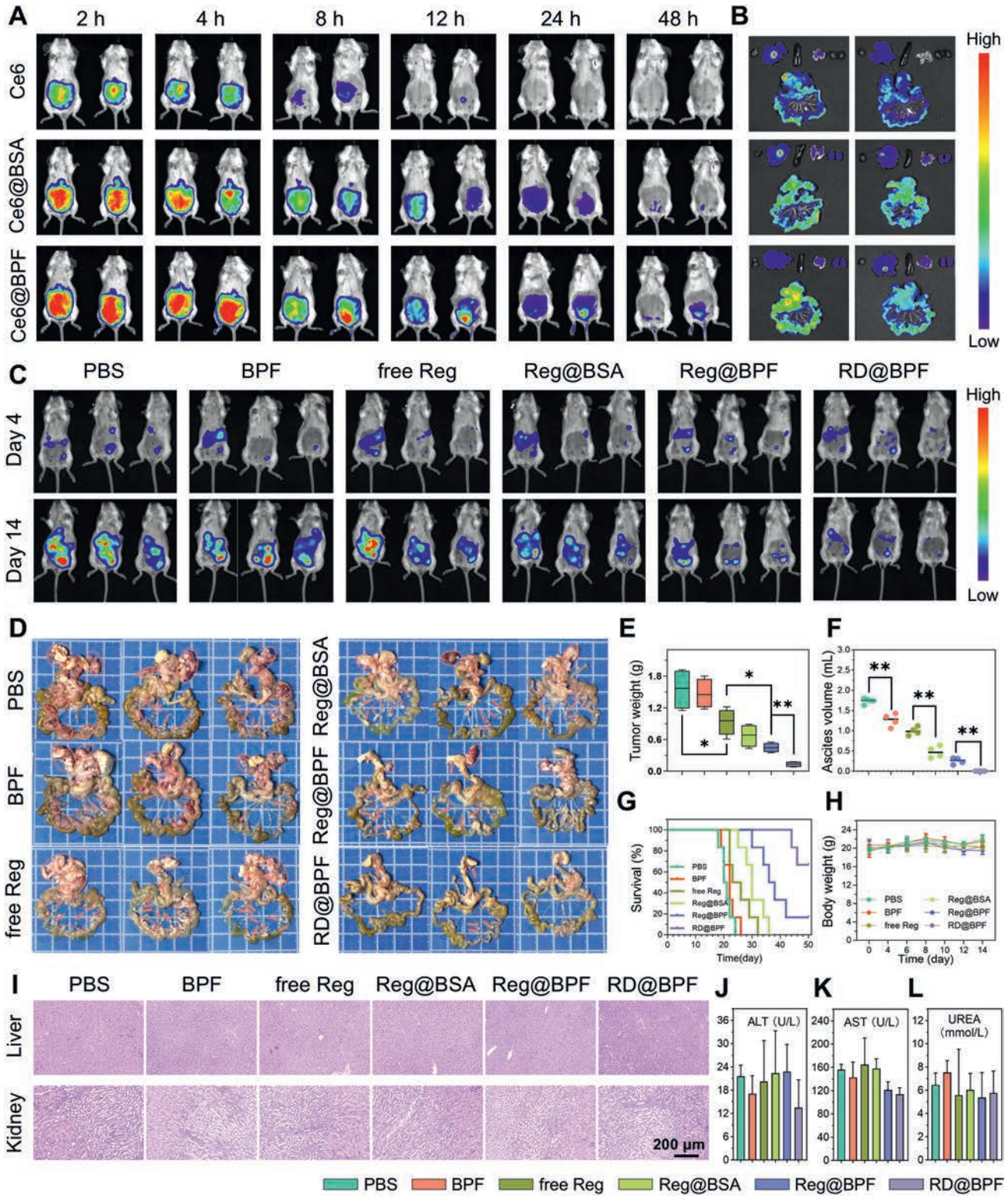

Figure 7 Reduction of tumor burden and suppression of ascites production by Reg/DMX@BPF NPs with high biosafety. (A) IVIS images of Ce6, Ce6@BSA NPs, and Ce6@BPF NPs at various time points after intraperitoneal injection ($n = 4$). (B) *Ex vivo* distribution of Ce6, Ce6@BSA NPs, and Ce6@BPF NPs in heart, liver, spleen, lung, kidney, and tumor tissues. (C) Bioluminescence images of tumor tissue after injection of D-Luciferin potassium salt. (D) Tumor metastatic nodules were observed on the gastrointestinal tract and mesentery. (E, F) Tumor weight and ascites volume across treatment groups ($n = 4$). (G) Survival condition of mice after various treatments ($n = 6$). (H) Body weight changes during treatment ($n = 4$). (I) H&E-stained sections of liver and kidney tissues (scale bar = 200 μm). (J–L) Serum levels of ALT, AST, and UREA across treatment groups ($n = 4$). The data are expressed as means ± SD. $^*P < 0.05$, $^{**}P < 0.01$. RD = Reg/DMX.

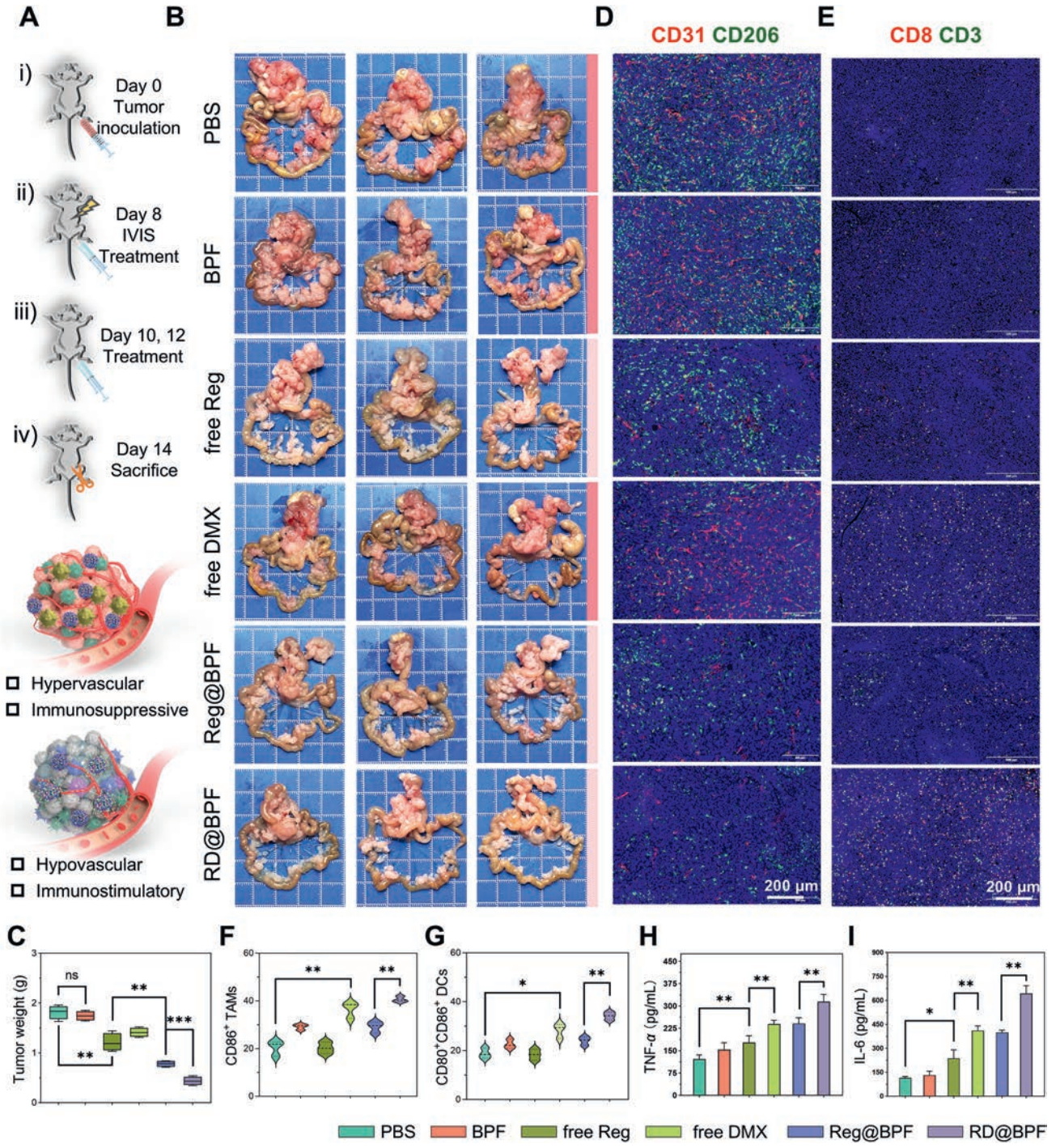

Figure 8 Inhibition of angiogenesis and reprogramming of immunosuppressive TME by Reg/DMX@BPF NPs. (A) Schematic diagram of intraperitoneal administration in peritoneal metastatic colorectal cancer mouse models, depicting TME changes after treatment. (B) Representative photographs of metastatic nodules in the gastrointestinal tract and mesentery. (C) Tumor weight per mouse across treatment groups ($n = 4$). (D) Immunofluorescence staining of $CD31^+$ vasculature and $CD206^+$ TAMs in tumor tissues (scale bar = 200 μm). (E) Immunofluorescence staining of infiltrating $CD3^+CD8^+$ T cells in tumor tissues (scale bar = 200 μm). (F) Flow cytometric quantification of $CD86^+$ TAMs in tumor tissue ($n = 3$). (G) Flow cytometric quantification of $CD80^+CD86^+$ DCs in spleen ($n = 3$). (H, I) Serum levels of TNF-α and IL-6 across treatment groups ($n = 3$). The data are expressed as means ± SD. $^{ns}P > 0.05$, $^{*}P < 0.05$, $^{**}P < 0.01$, $^{***}P < 0.001$. RD = Reg/DMX.

post-inoculation (Fig. 8A). Despite the advanced tumor stage, Reg/DMX@BPF NPs exhibited exceptional control, reducing tumor burden to 0.44 ± 0.08 g, a 7.5-fold decrease compared to PBS controls (1.82 ± 0.14 g), and significantly outperforming all monotherapy groups (Fig. 8C). Malignant ascites was nearly eliminated in the combination group (0.24 ± 0.07 mL), in stark contrast to the significant fluid accumulation in PBS-treated mice (1.81 ± 0.16 mL). The blank BPF carrier alone showed a modest

reduction in ascites, while Reg@BPF NPs demonstrated superior tumor suppression over free Reg, underscoring the importance of nanocarrier-mediated delivery (Supporting Information Fig. S6A).

The antitumor effect was underpinned by a synergistic mechanism targeting both the vascular and immune compartments of the TME. Macroscopically, tumors from Reg-treated groups appeared pale and hypovascular (Fig. 8B). Immunofluorescence staining further elucidated these effects, showing that PBS-treated tumors were replete with $CD31^+$ vascular structures and $CD206^+$ M2 TAMs (Fig. 8D), hallmarks of a pro-tumorigenic, immunosuppressive niche. Reg primarily inhibited $CD31^+$ vessel formation, while DMX treatment markedly depleted M2 TAMs (Fig. S6B and S6D). Furthermore, CD31/αSMA co-staining revealed that Reg/DMX@BPF NPs significantly promoted vascular normalization, evidenced by a marked increase in pericyte coverage (74.44 $\pm$ 12.82%) compared to the PBS group (9.20 $\pm$ 2.76%) (Fig. S6C and S6F), indicating functional improvement of tumor vessels.

Concurrently, the nanoplatform induced profound immune reprogramming. Gating strategies for TAMs and DCs analyses are provided in Fig. S6G and S6I, respectively. Flow cytometry showed that Reg/DMX@BPF NPs significantly increased the proportion of anti-tumor M1 TAMs ($CD86^+$) within tumors (40.62 $\pm$ 1.11% *vs.* 20.48 $\pm$ 3.09% in PBS controls; Fig. 8F, Fig. S6H) and enhanced the population of mature DCs ($CD80^+CD86^+$) in the spleen (34.16 $\pm$ 1.69% *vs.* 18.82 $\pm$ 2.12%; Fig. 8G, Fig. S6J). This remodeling of the immunosuppressive TME was accompanied by robust infiltration of $CD3^+CD8^+$ T cells into tumor nests (Fig. 8E, Fig. S6E), suggesting the establishment of an immunostimulatory milieu. These localized changes were consistent with systemic immune activation. Reg/DMX@BPF NPs group exhibited the highest serum levels of TNF-α (314.04 $\pm$ 24.65 pg/mL) and IL-6 (642.80 $\pm$ 49.56 pg/mL), significantly surpassing monotherapy groups (Fig. 8H and I). The pronounced cytokine response, together with enhanced cytotoxic T cell infiltration and M2 TAM reduction, underscores a reinforced antitumor immune response.

4. Discussion

Anti-angiogenic therapy fundamentally aims to inhibit the formation of tumor neovasculature, thereby depriving tumors of essential nutrients and oxygen supplies to curtail their progression[48]. However, the clinical efficacy of anti-angiogenic therapy in PMC is severely limited by the ensuing immunosuppressive TME and drug delivery barriers[31,49-51]. In this study, we developed a novel nanoplatform (Reg/DMX@BPF NPs) that co-delivers Reg and DMX to simultaneously target these intertwined challenges. Our key findings demonstrate that this strategy not only achieves superior tumor accumulation and penetration through dual-ligand targeting but also, more importantly, successfully disrupts the vascular-immune vicious cycle, as evidenced by the significant suppression of tumor growth (92% reduction) and ascites formation *in vivo*.

Our approach introduces several key innovations over existing strategies. First, the poor aqueous solubility and aggregation tendency of the STING agonist DMX have impeded its clinical translation[52]. Inspired by the carrier-free self-assembled nanoparticles[53-55], we repurposed Reg as a molecular scaffold. As confirmed by FTIR and XRD analyses, Reg effectively prevents DMX aggregation *via* $\pi-\pi$ stacking, leading to the formation of stable, amorphous nanoparticles with high drug-loading capacity (Reg: 77.6 $\pm$ 1.2%; DMX: 64.3 $\pm$ 1.4%). Second, passive diffusion remains inadequate for effective intraperitoneal therapy. To overcome this, we incorporated active targeting ligands, FA for selective tumor cell uptake and PBA for enrichment at metastatic sites through binding to SA. Our *in vivo* biodistribution results unequivocally showed that the BPF modification significantly enhanced nanoparticles accumulation in peritoneal tumors compared to non-targeted BSA NPs or free drug, which is a crucial factor for improving therapeutic efficacy while reducing systemic exposure.

Notably, the BPF nanocarrier exerts multifaceted effects that extend beyond mere drug delivery, which is a key advancement of our system. The strategic inclusion of PBA converts the lysosome from a degradative compartment into a controlled release portal[56]. The lysosomal escape experiments provided direct evidence: BPF NPs exhibited a dramatic shift from lysosomal colocalization (PCC = 0.45 $\pm$ 0.10 at 4 h) to cytoplasmic dispersion (PCC = 0.27 $\pm$ 0.03 at 8 h), accompanied by acridine orange signal loss in the APC channel, indicating membrane permeabilization. This boronate ester-mediated mechanism surpasses the efficiency of conventional nanocarriers, which often depend on suboptimal osmotic lysis or the proton sponge effect for lysosomal escape[57,58]. Moreover, a particularly novel finding of our study is the intrinsic immunostimulatory role of the BPF nanocarrier itself. While previous studies have modified BSA for targeting, few have reported the carrier itself as a potent immune activator[59-63]. Our study revealed that BPF, likely due to the covalent modification creating PAMP-like structures, potently activated TLR4/NF-κB signaling, promoted M1 polarization of TAMs, and enhanced DC maturation. This duality underscores the promising potential of nanomedicines, where carriers serve as co-therapeutics, while also emphasizing that this unique property demands careful evaluation, particularly in inflammation-prone contexts.

5. Conclusions

In summary, this study extends beyond conventional formulation optimization by integrating multidimensional therapeutics into a unified nanoplatform with precise targeting and intracellular trafficking capabilities. Reg/DMX@BPF NPs simultaneously disrupted angiogenesis and alleviated immunosuppression through STING activation and BPF-induced TLR4 signaling. The pronounced suppression of tumor growth and ascites formation, combined with high drug-loading efficiency, durable stability, and an excellent biosafety profile, highlights Reg/DMX@BPF NPs as a promising therapeutic candidate for PMC. The clinical precedence of BSA and Reg, coupled with their innovative modification, enhances the platform's translational potential[64-66]. Ultimately, this work not only furnishes a promising therapeutic for PMC but also establishes a conceptual framework for engineering a nanoplatform that integrates active co-therapeutic carriers with rational drug combinations to reshape the TME.

Ethics approval

All animal experiments were approved by the Experimental Animal Ethics Committee of the State Key Laboratory of Biotherapy, Sichuan University (Approval No. 20241127009) and performed in accordance with AAALAC International standards for laboratory animal welfare.

Acknowledgments

This study was supported by the National Natural Science Foundation of China (NSFC32530059), Natural Science Foundation of Sichuan Province (No. 2024NSFSC0046, China), and 135 Project for Disciplines of Excellence, West China Hospital, Sichuan University (No. ZYGD24003, China).

Author contributions

Meng Wang: Conceptualization, Methodology, Investigation, Visualization, Writing. Yutong Qian: Methodology, Investigation, Writing. Yicong Li: Methodology, Visualization. Xicheng Li: Resources. Mei Zhu: Investigation, Data curation. Danrong Hu: Supervision, Validation. Ran Li: Supervision, Project administration. Meng Pan: Resources, Formal analysis. Yun Yang: Validation, Data curation. Jianan Li: Resources. Zhiyong Qian: Conceptualization, Funding acquisition, Writing.

Conflicts of interest

The authors declare no conflicts of interest.

Appendix A. Supporting information

Supporting information to this article can be found online at https://doi.org/10.1016/j.apsb.2026.04.016.

References

1. van Gestel YR, de Hingh IH, van Herk-Sukel MP, van Erning FN, Beerepoot LV, Wijsman JH, et al. Patterns of metachronous metastases after curative treatment of colorectal cancer. *Cancer Epidemiol* 2014; **38**:448−54.
2. Segelman J, Granath F, Holm T, Machado M, Mahteme H, Martling A. Incidence, prevalence and risk factors for peritoneal carcinomatosis from colorectal cancer. *Br J Surg* 2012;**99**:699−705.
3. Klaver YL, Lemmens VE, Nienhuijs SW, Luyer MD, de Hingh IH. Peritoneal carcinomatosis of colorectal origin: incidence, prognosis and treatment options. *World J Gastroenterol* 2012;**18**:5489−94.
4. Sluiter N, de Cuba E, Kwakman R, Kazemier G, Meijer G, Te Velde EA. Adhesion molecules in peritoneal dissemination: function, prognostic relevance and therapeutic options. *Clin Exp Metastasis* 2016;**33**:401−16.
5. Lemoine L, Sugarbaker P, Van der Speeten K. Pathophysiology of colorectal peritoneal carcinomatosis: role of the peritoneum. *World J Gastroenterol* 2016;**22**:7692−707.
6. Cantor JR, Sabatini DM. Cancer cell metabolism: one hallmark, many faces. *Cancer Discov* 2012;**2**:881−98.
7. Elias D, Gilly F, Boutitie F, Quenet F, Bereder J-M, Mansvelt B, et al. Peritoneal colorectal carcinomatosis treated with surgery and perioperative intraperitoneal chemotherapy: retrospective analysis of 523 patients from a multicentric French study. *J Clin Oncol* 2009;**28**:63−8.
8. Parikh MS, Johnson P, Romanes JP, Freitag HE, Spring ME, Garcia-Henriquez N, et al. Cytoreductive surgery and hyperthermic intraperitoneal chemotherapy for colorectal peritoneal metastases: a systematic review. *Dis Colon Rectum* 2022;**65**:16−26.
9. Ferrara N, Adamis AP. Ten years of anti-vascular endothelial growth factor therapy. *Nat Rev Drug Discov* 2016;**15**:385−403.
10. Guelfi S, Hodivala-Dilke K, Bergers G. Targeting the tumour vasculature: from vessel destruction to promotion. *Nat Rev Cancer* 2024;**24**: 655−75.
11. Mahdi A, Darvishi B, Majidzadeh AK, Salehi M, Farahmand L. Challenges facing antiangiogenesis therapy: the significant role of hypoxia-inducible factor and MET in development of resistance to anti-vascular endothelial growth factor-targeted therapies. *J Cell Physiol* 2019;**234**:5655−63.
12. Rivera LB, Bergers G. Intertwined regulation of angiogenesis and immunity by myeloid cells. *Trends Immunol* 2015;**36**:240−9.
13. Carmeliet P, Jain RK. Principles and mechanisms of vessel normalization for cancer and other angiogenic diseases. *Nat Rev Drug Discov* 2011;**10**:417−27.
14. Li Q, Zeng K, Chen Q, Han C, Wang X, Li B, et al. Atractylenolide I inhibits angiogenesis and reverses sunitinib resistance in clear cell renal cell carcinoma through ATP6V0D2-mediated autophagic degradation of EPAS1/HIF2α. *Autophagy* 2025;**21**:619−38.
15. Ellis LM, Hicklin DJ. VEGF-targeted therapy: mechanisms of anti-tumour activity. *Nat Rev Cancer* 2008;**8**:579−91.
16. Pardoll DM. The blockade of immune checkpoints in cancer immunotherapy. *Nat Rev Cancer* 2012;**12**:252−64.
17. Kuo HY, Khan KA, Kerbel RS. Antiangiogenic-immune-checkpoint inhibitor combinations: lessons from phase III clinical trials. *Nat Rev Clin Oncol* 2024;**21**:468−82.
18. Gabrilovich DI, Nagaraj S. Myeloid-derived suppressor cells as regulators of the immune system. *Nat Rev Immunol* 2009;**9**:162−74.
19. Strauss L, Bergmann C, Szczepanski M, Gooding W, Johnson JT, Whiteside TL. A unique subset of $CD4^{+}CD25highFoxp3^{+}$ T cells secreting interleukin-10 and transforming growth factor-beta1 mediates suppression in the tumor microenvironment. *Clin Cancer Res* 2007;**13**:4345−54.
20. Noy R, Pollard JW. Tumor-associated macrophages: from mechanisms to therapy. *Immunity* 2014;**41**:49−61.
21. Hongu T, Pein M, Insua-Rodríguez J, Gutjahr E, Mattavelli G, Meier J, et al. Perivascular tenascin C triggers sequential activation of macrophages and endothelial cells to generate a pro-metastatic vascular niche in the lungs. *Nat Cancer* 2022;**3**:486−504.
22. Motz GT, Coukos G. Deciphering and reversing tumor immune suppression. *Immunity* 2013;**39**:61−73.
23. Kastelein AW, Vos LMC, van Baal J, Koning JJ, Hira VVV, Nieuwland R, et al. Poor perfusion of the microvasculature in peritoneal metastases of ovarian cancer. *Clin Exp Metastasis* 2020;**37**:293−304.
24. Yang H, Lee WS, Kong SJ, Kim CG, Kim JH, Chang SK, et al. STING activation reprograms tumor vasculatures and synergizes with VEGFR2 blockade. *J Clin Investig* 2019;**129**:4350−64.
25. Grothey A, Cutsem EV, Sobrero A, Siena S, Falcone A, Ychou M, et al. Regorafenib monotherapy for previously treated metastatic colorectal cancer (CORRECT): an international, multicentre, randomised, placebo-controlled, phase 3 trial. *Lancet* 2013;**381**:303−12.
26. Flood BA, Higgs EF, Li S, Luke JJ, Gajewski TF. STING pathway agonism as a cancer therapeutic. *Immunol Rev* 2019;**290**:24−38.
27. Chen Z, Meng CY, Mai JH, Liu YB, Li HW, Shen HF. An mRNA vaccine elicits STING-dependent antitumor immune responses. *Acta Pharm Sin B* 2023;**13**:1274−86.
28. Downey CM, Aghaei M, Schwendener RA, Jirik FR. DMXAA causes tumor site-specific vascular disruption in murine non-small cell lung cancer, and like the endogenous non-canonical cyclic dinucleotide STING agonist, 2′3′-cGAMP, induces M2 macrophage repolarization. *PLoS One* 2014;**9**:e99988.
29. Gao P, Ascano M, Zillinger T, Wang W, Dai P, Serganov AA, et al. Structure−function analysis of STING activation by c[G(2′,5′)pA(3′,5′)p] and targeting by antiviral DMXAA. *Cell* 2013; **154**:748−62.
30. Liu Y, Crowe WN, Wang L, Lu Y, Petty WJ, Habib AA, et al. An inhalable nanoparticulate STING agonist synergizes with radiotherapy to confer long-term control of lung metastases. *Nat Commun* 2019;**10**: 5108.
31. van Stein RM, Aalbers AGJ, Sonke GS, van Driel WJ. Hyperthermic intraperitoneal chemotherapy for ovarian and colorectal cancer: a review. *JAMA Oncol* 2021;**7**:1231−8.
32. Chen X, Tang Q, Wang J, Zhou Y, Li F, Xie Y, et al. A DNA/DMXAA/metal-organic framework activator of innate immunity for boosting anticancer immunity. *Adv Mater* 2023;**35**:e2210440.

33. Xu X, Ho W, Zhang X, Bertrand N, Farokhzad O. Cancer nanomedicine: from targeted delivery to combination therapy. *Trends Mol Med* 2015;**21**:223−32.
34. Taghipour YD, Zarebkohan A, Salehi R, Rahimi F, Torchilin VP, Hamblin MR, et al. An update on dual targeting strategy for cancer treatment. *J Control Release* 2022;**349**:67−96.
35. Zhao LP, Huang CY, Zheng RR, Zhou HY, Chen GM, Ye Y, et al. Cu^{2+}-coordinated NLG919: a drug delivery nanoplatform to activate antitumor immunity *via* inducing immunogenic cell death and inhibiting indoleamine 2,3-dioxygenase-1. *MedComm Biomater Appl* 2025; **4**:e70024.
36. Chen W, Shi K, Yu Y, Yang PP, Bei ZW, Mo D, et al. Drug delivery systems for colorectal cancer chemotherapy. *Chinese Chem Lett* 2024; **35**:109159.
37. Shen X, Liu X, Li T, Chen Y, Chen Y, Wang P, et al. Recent advancements in serum albumin-based nanovehicles toward potential cancer diagnosis and therapy. *Front Chem* 2021;**9**:746646.
38. Zhang Y, Sun T, Jiang C. Biomacromolecules as carriers in drug delivery and tissue engineering. *Acta Pharm Sin B* 2018;**8**: 34−50.
39. Verwaal VJ, van Tinteren H, van Ruth S, Fan Zoetmulder. Predicting the survival of patients with peritoneal carcinomatosis of colorectal origin treated by aggressive cytoreduction and hyperthermic intraperitoneal chemotherapy. *Br J Surg* 2004;**91**:739−46.
40. Li J, Wu HB, Li HY, Zhang Y, Zhang HJ, Wang L, et al. Hemoglobin nanocatalyst with tunable autoxidation activity for tumor apoptosis-ferroptosis combination therapy. *Acta Pharm Sin B* 2025;**15**: 6626−37.
41. Assaraf YG, Leamon CP, Reddy JA. The folate receptor as a rational therapeutic target for personalized cancer treatment. *Drug Resist Updates* 2014;**17**:89−95.
42. Wang SM, Ma D, Yang MH, Zhang Y, Wang SF, Zhou WH. Arsenic trioxide-based nanoparticles for enhanced chemotherapy by activating pyroptosis. *Acta Pharm Sin B* 2025;**15**:6001−18.
43. Qian X, Ge L, Yuan K, Li C, Zhen X, Cai W, et al. Targeting and microenvironment-improving of phenylboronic acid-decorated soy protein nanoparticles with different sizes to tumor. *Theranostics* 2019; **9**:7417−30.
44. Xiong L, Chen S, Li SH, He D, Wang YS, Zhang Q, et al. ATP-responsive tumor targeted lipid nanoparticle for enhanced siRNA delivery and improved treatment efficacy in melanoma. *J Control Release* 2025;**382**:113622.
45. Wang R, Yin C, Liu C, Sun Y, Xiao P, Li J, et al. Phenylboronic acid modification augments the lysosome escape and antitumor efficacy of a cylindrical polymer brush-based prodrug. *J Am Chem Soc* 2021;**143**: 20927−38.
46. Zhang Q, Liu Y, Fei Y, Xie J, Zhao X, Zhong Z, et al. Phenylboronic acid-functionalized copolypeptides: facile synthesis and responsive dual anticancer drug release. *Biomacromolecules* 2022;**23**: 2989−98.
47. Wang LL, He SS, Liu R, Xue Y, Quan Y, Shi RY, et al. A pH/ROS dual-responsive system for effective chemoimmunotherapy against melanoma *via* remodeling tumor immune microenvironment. *Acta Pharm Sin B* 2024;**14**:2263−80.
48. Yang J, Wang Q, Qiao C, Lin Z, Li X, Huang Y, et al. Potent anti-angiogenesis and anti-tumor activity of a novel human anti-VEGF antibody, MIL60. *Cell Mol Immunol* 2014;**11**:285−93.
49. Jain RK. Antiangiogenesis strategies revisited: from starving tumors to alleviating hypoxia. *Cancer Cell* 2014;**26**:605−22.
50. Lv S, Liu Y, Xie C, Xue C, Du S, Yao J. Emerging role of interactions between tumor angiogenesis and cancer stem cells. *J Control Release* 2023;**360**:468−81.
51. Dai J, Ji C. In-depth size and charge variants characterization of monoclonal antibody with native mass spectrometry. *Anal Chim Acta* 2023;**1265**:341360.
52. Chen M, Wang C, Wang X, Tu Z, Ding Z, Liu Z. An "AND" logic-gated prodrug micelle locally stimulates antitumor immunity. *Adv Mater* 2024;**36**:e2307818.
53. Su Q, Wang Z, Zhou H, Zhang M, Deng W, Wei X, et al. Eradication of large tumors by nanoscale drug self-assembly. *Adv Mater* 2024;**36**: e2410536.
54. Gao S, Zheng H, Xu S, Kong J, Gao F, Wang Z, et al. Novel natural carrier-free self-assembled nanoparticles for treatment of ulcerative colitis by balancing immune microenvironment and intestinal barrier. *Adv Healthcare Mater* 2023;**12**:e2301826.
55. Shen J, Chen L, Lv X, Liu N, Miao Y, Zhang Q, et al. Emerging co-assembled and sustained released natural medicinal nanoparticles for multitarget therapy of choroidal neovascularization. *Adv Mater* 2024; **36**:e2314095.
56. Lim J, Lee J, Jung S, Kim WJ. Phenylboronic-acid-based nanocomplex as a feasible delivery platform of immune checkpoint inhibitor for potent cancer immunotherapy. *J Control Release* 2021;**330**: 1168−77.
57. Ahmad A, Khan JM, Haque S. Strategies in the design of endosomolytic agents for facilitating endosomal escape in nanoparticles. *Biochimie* 2019;**160**:61−75.
58. Varkouhi AK, Scholte M, Storm G, Haisma HJ. Endosomal escape pathways for delivery of biologicals. *J Control Release* 2011;**151**: 220−8.
59. Nosrati H, Abbasi R, Charmi J, Rakhshbahar A, Aliakbarzadeh F, Danafar H, et al. Folic acid conjugated bovine serum albumin: an efficient smart and tumor targeted biomacromolecule for inhibition folate receptor positive cancer cells. *Int J Biol Macromol* 2018;**117**: 1125−32.
60. Hsu WH, Ku CL, Lai YR, Wang SS, Chou SH, Lin TH. Developing targeted drug delivery carriers for breast cancer using glutathione-sensitive doxorubicin-coupled glycated bovine serum albumin nanoparticles. *Int J Biol Macromol* 2023;**249**:126114.
61. Zhao D, Zhao X, Zu Y, Li J, Zhang Y, Jiang R, et al. Preparation, characterization, and in vitro targeted delivery of folate-decorated paclitaxel-loaded bovine serum albumin nanoparticles. *Int J Nanomed* 2010;**5**:669−77.
62. Wang S, Guo Q, Xu R, Lin P, Deng G, Xia X. Combination of ferroptosis and pyroptosis dual induction by triptolide nano-MOFs for immunotherapy of melanoma. *J Nanobiotechnol* 2023;**21**:383.
63. Wang L, Wu Y, Yang N, Yin W, Yang H, Li C, et al. Self-assembly of maltose-albumin nanoparticles for efficient targeting delivery and therapy in liver cancer. *Int J Biol Macromol* 2024;**258**:128691.
64. Grothey A, Van Cutsem E, Sobrero A, Siena S, Falcone A, Ychou M, et al. Regorafenib monotherapy for previously treated metastatic colorectal cancer (CORRECT): an international, multicentre, randomised, placebo-controlled, phase 3 trial. *Lancet* 2013;**381**:303−12.
65. An FF, Zhang XH. Strategies for preparing albumin-based nanoparticles for multifunctional bioimaging and drug delivery. *Theranostics* 2017;**7**:3667−89.
66. Solanki R, Rostamabadi H, Patel S, Jafari SM. Anticancer nanodelivery systems based on bovine serum albumin nanoparticles: a critical review. *Int J Biol Macromol* 2021;**193**:528−40.